South Atlantic Ocean and air-sea interaction

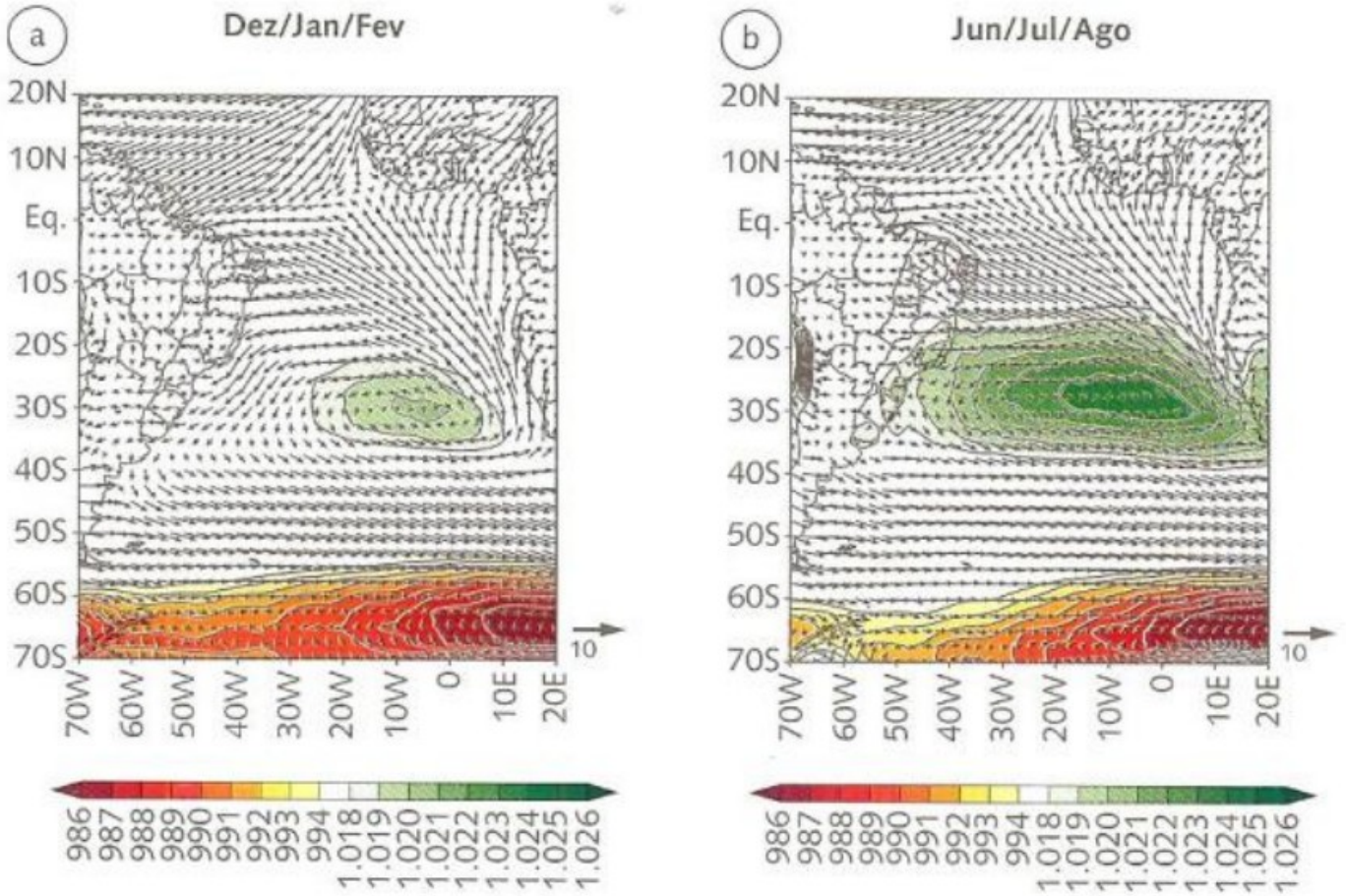

Fig. 24.2 Sistemas de alta (verde) e baixa (vermelho) pressão atmosférica ao nível médio do mar e vento em 1.000 hPa sobre o oceano Atlântico Sul. Figuras geradas a partir dos dados de reanálise NCEP/NCAR
Fonte: Kalnay et al., 1996.

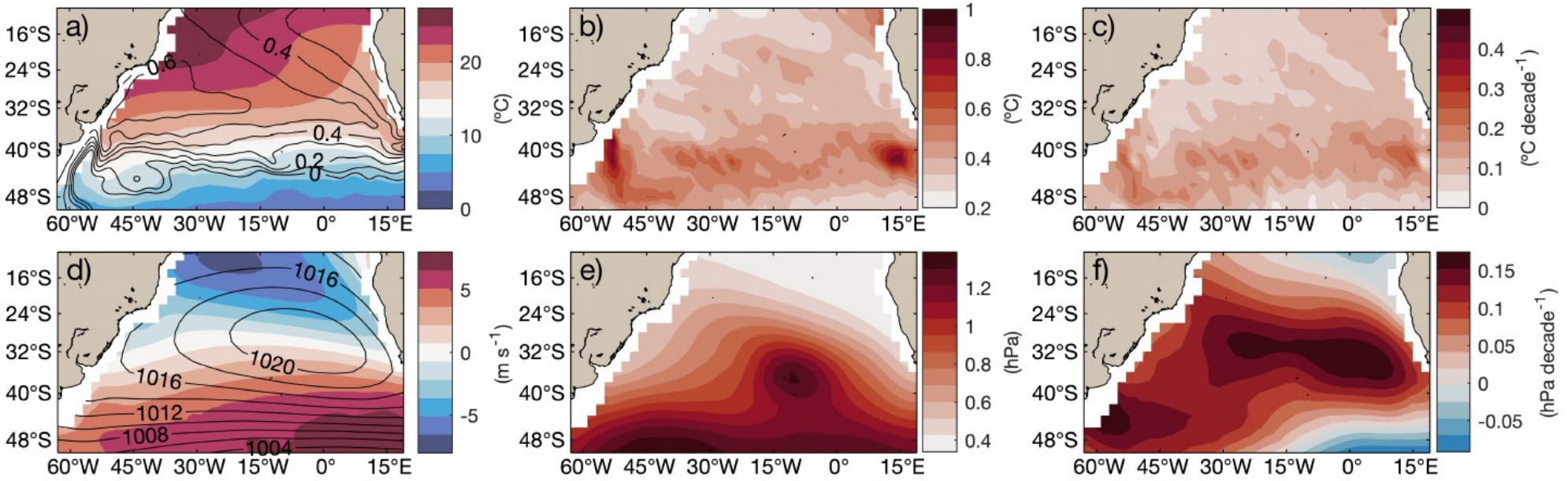

Figure 1. Climatological properties of surface fields in the South Atlantic domain of this study. a) Mean SST (ºC) and absolute dynamic topography (ADT; m) in shades and contours, respectively. b) Interannual standard deviation of SST (ºC). c) Linear trend of SST (ºC/decade). d) Mean zonal wind (ms^{-1}) and sea level pressure (SLP) in shades and contours, respectively. e) Interannual standard deviation of SLP (hPa). f) Linear trend of SLP (hPa/decade).

Manta et al 2024

Corrientes geostróficas en superficie

En superficie esas ecuaciones
se pueden escribir como

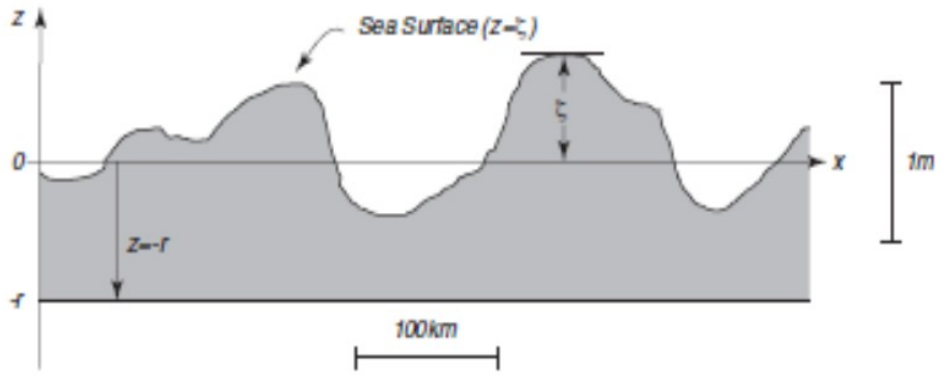

$$v = \frac{g}{f}\frac{\partial \eta}{\partial x}$$

$$u = \frac{-g}{f}\frac{\partial \eta}{\partial y}$$

η = altura del
nivel del mar

PETERSON e Stramma (1991) descreveram o sistema de correntes do oceano Atlântico Sul por meio de sua circulação geostrófica superficial (Fig. 24.1), dominada por um sistema de giros subtropicais anticiclônicos (anti-horário no Hemisfério Sul), pelos sistemas de correntes equatoriais e pela Corrente Circumpolar Antártica (CCA). As correntes marinhas que dominam esses sistemas são: 1) Corrente Sul Equatorial (CSE); 2) Corrente do Brasil (CB); 3) Corrente das Malvinas (CM), 4) Corrente Sul Atlântica (CSA); e 5) Corrente de Benguela.

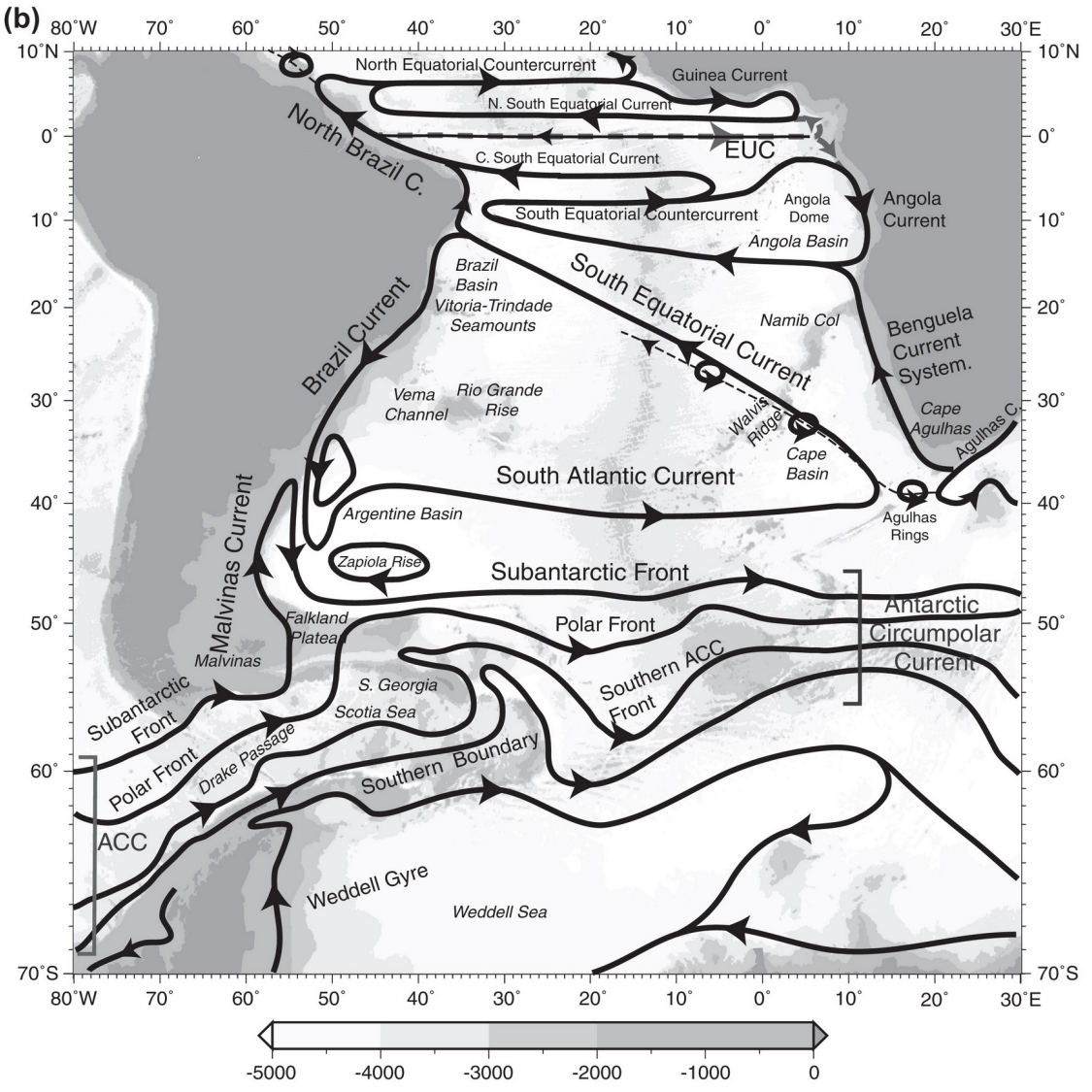

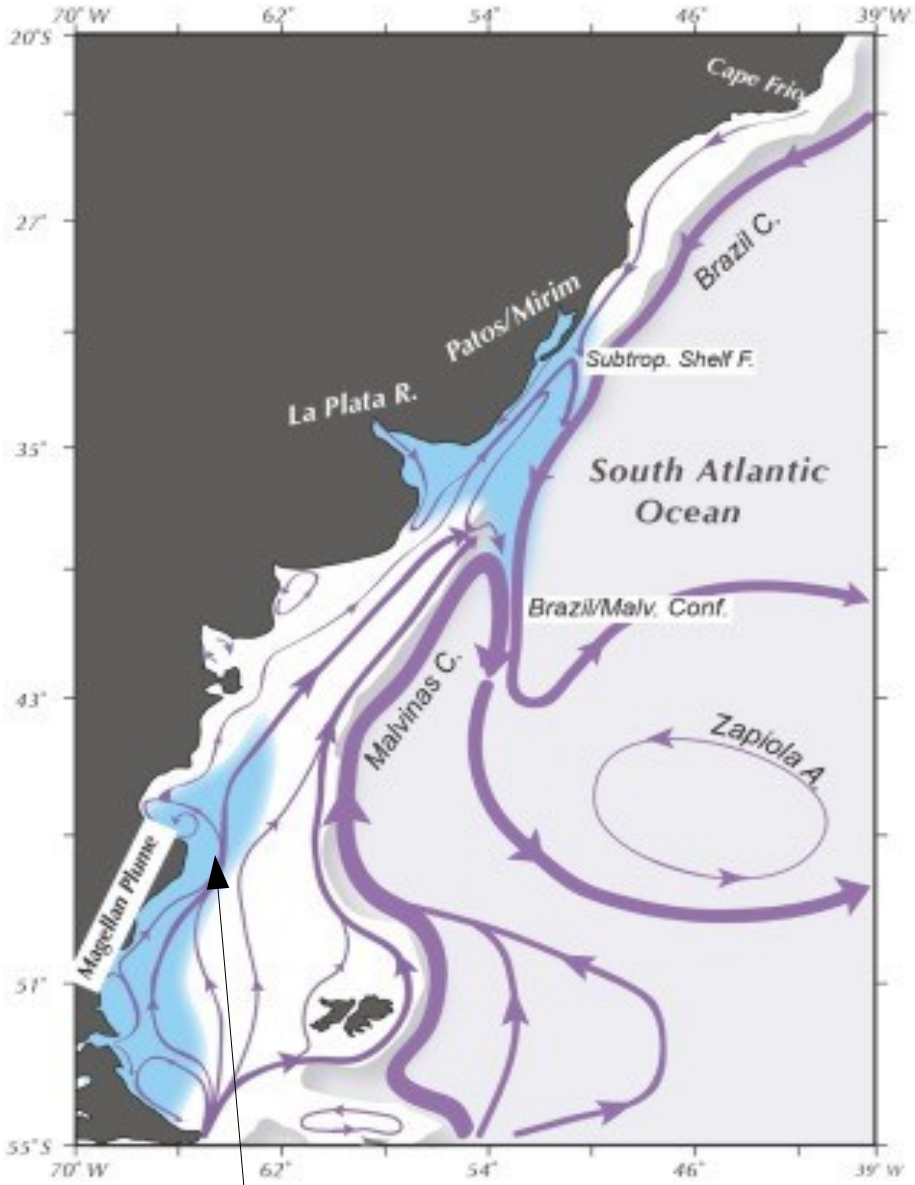

Corriente de Patagonia

NA PARTE oeste do oceano Atlântico Sul, conhecida como oceano Atlântico Sudoeste, as Águas Costeiras (AC) originadas por ação da descarga continental adicionam complexidade ao sistema. Embora sempre presente, as AC têm índices termoalinos variáveis em função da estação do ano e local. De acordo com Garcia (1997), essa variação depende sobretudo das descargas do rio da Prata (34°S a 37°S; 54°W a 58.5°W) e da lagoa dos Patos (30°S a 32°S; 50°W a 52°W), que contribuem para tornar a estrutura vertical das águas do oceano Atlântico Sudoeste muito complexa.

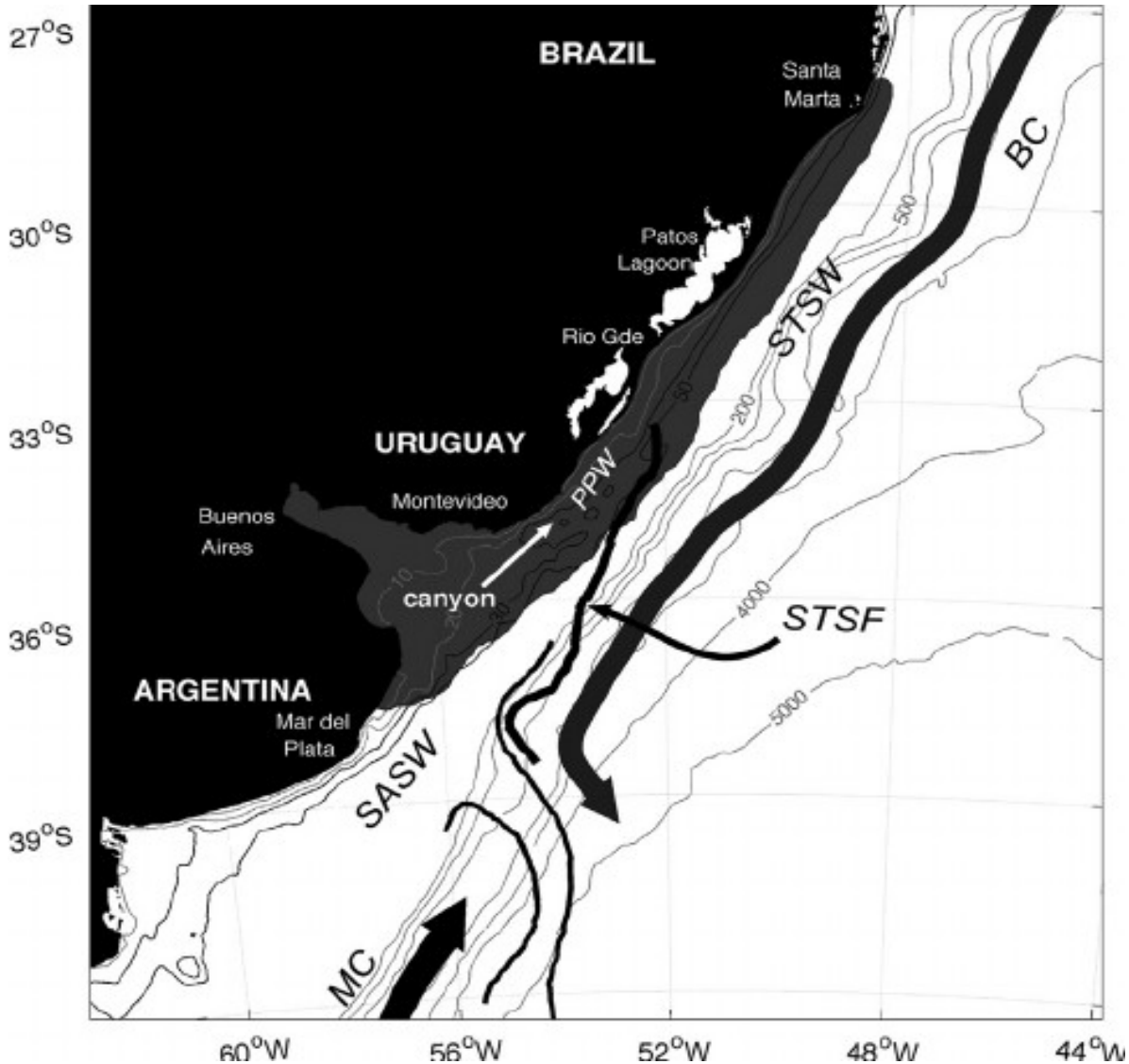
27°S
30°S
33°S
36°S
39°S
60°W
56°W
52°W
48°W
44°W
BRAZIL
Santa Marta
Patos Lagoon
Rio Gde
URUGUAY
Montevideo
Buenos Aires
canyon
ARGENTINA
Mar del Plata
BC
STSW
STSF
PPW
SASW
MC
50
200
500
4000
5000

Bajo la capa superficial en contacto con la atmósfera, T y S se conservan permitiendo la identificación de masas de agua.

T y S lejos de la superficie solo pueden cambiar a través de la fricción y advección.

- Algunas masas de agua
  - Aguas Profundas del Atlántico Norte (NADW)
    - T=2-4 C, S=34.9-35
  - Aguas Antarticas de Fondo (AABW)
    - T=-0.5-0 C, S=34.6-34.7
  - Aguas Antárticas Intermedias (AAIW)
    - T=3.0-4.0 C, S=34.2-34.3

Subtropical Front

Subantarctic Front

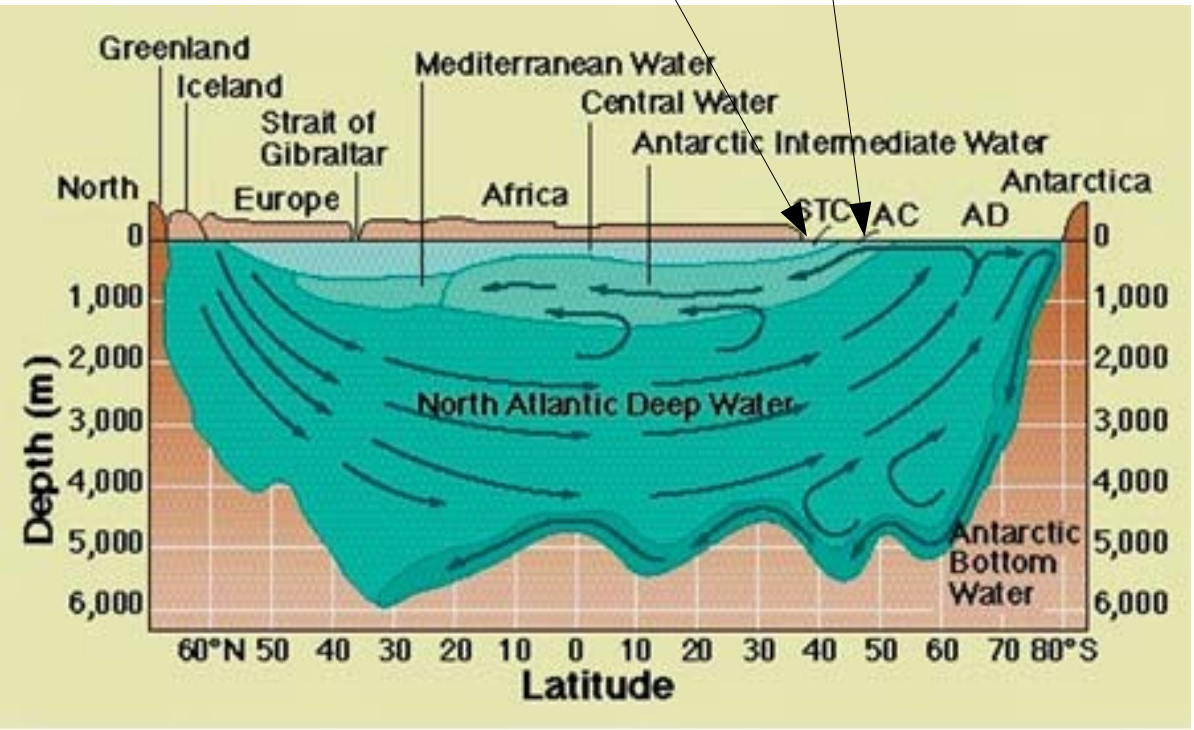

The water layers and deep circulation of the Atlantic Ocean. Arrows on this diagram indicate the direction of water movement. STC indicates the position of the Subtropical Convergence, AC the Antarctic Convergence, and AD the Antarctic Divergence. The surface layer is too thin to show clearly in this scale

SVERDRUP, Johnson e Feming (1942) estabeleceram as características termoalinas da Água Tropical (AT), que é transportada pela CB em superfície desde a sua região de formação. Emilson (1961) e Thomsen (1962) propuseram novos índices termoalinos com os limites de $T > 20°C$; $S > 36$ (Emilson, 1961). Nos níveis abaixo da superfície até o fundo, as massas de água do oceano Atlântico Sul são a Água Central do Atlântico Sul (ACAS), a Água Antártica Intermediária (AAI), a Água Profunda do Atlântico Norte (APAN) e a Água Antártica de Fundo (AAF).

Cálculo de corrientes en profundidad

Usamos el viento térmico: cambio de la velocidad geostrófica con la profundidad

Mediciones hidrográficas de T y S permiten calcular ρ

Es necesario elegir un nivel de referencia.

$$\frac{\partial u_g}{\partial z} = \frac{g}{\rho_0 f}\frac{\partial \rho}{\partial y}$$

$$\frac{\partial v_g}{\partial z} = \frac{-g}{\rho_0 f}\frac{\partial \rho}{\partial x}$$

Integrando entre z1 y z2 podemos obtener el cambio de velocidad de las corrientes como

$$f(v_2 - v_1) = g\frac{\partial h'}{\partial x}$$

$$f(u_2 - u_1) = -g\frac{\partial h'}{\partial y}$$

$$h' = -\left(\frac{1}{\rho_0}\right)\int \rho\, dz$$

El nivel z1 es el nivel de referencia. En general se considera que z1 representa un nivel de no movimiento (~2000m).

Una mejor alternativa es considerar un nivel donde se conoce la velocidad de las corrientes en base a mediciones in-situ.

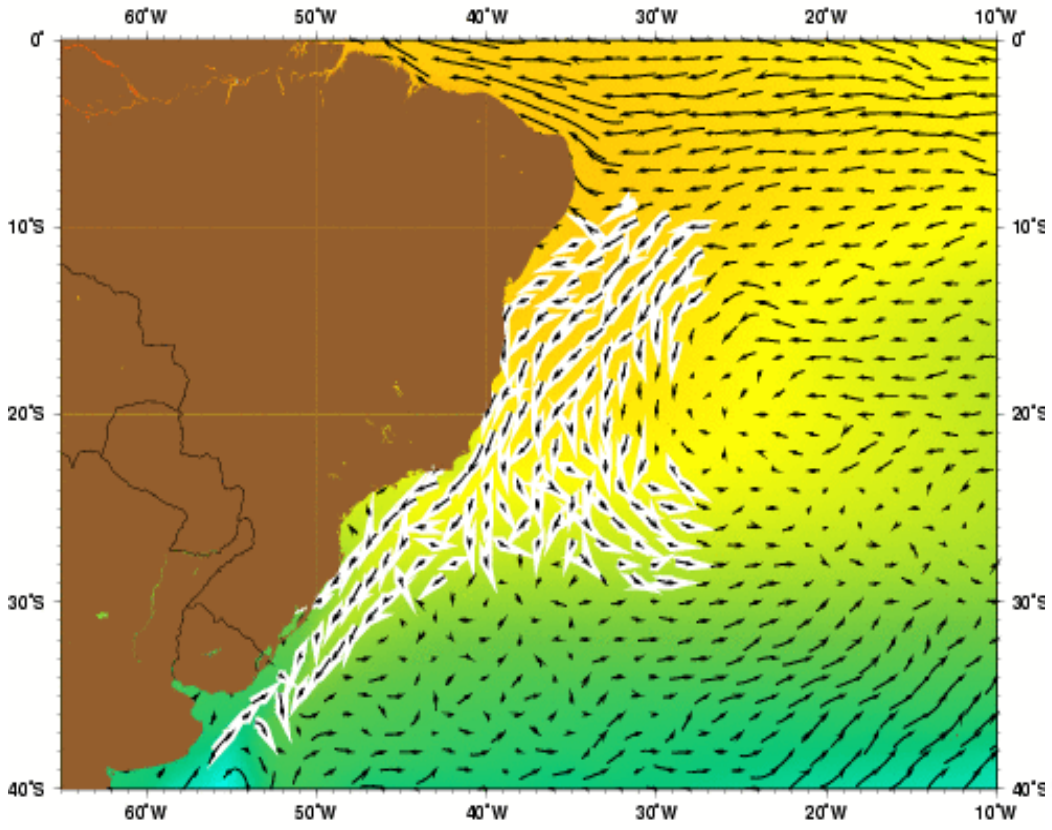

Conforme Peterson e Stramma (1991), a CB é uma corrente de contorno oeste formada nas latitudes próximas a 10°S, alimentada por uma pequena porção (cerca de 4 Sv) da CSE que se bifurca na direção sul. Os autores sugerem que a CB permanece com um transporte relativamente pequeno (cerca de 11 Sv ou menos) ao longo de sua trajetória para o sul entre 19°S e 25°S. Garfield (1990), no entanto, descreve que o transporte da CB aumenta ao sul de Cabo Frio em 23°S. Gordon e Greengrove (1986) relatam também que a taxa de intensificação do transporte da CB ao sul de Cabo Frio é de cerca de 5% por 100 km.

Garfield (1990) descreve a CB abaixo de 24°S como uma corrente estreita e rasa, transportando AT e ACAS em profundidades menores que 400 m. Em 31°S, a CB torna-se mais larga e profunda, e os mecanismos disso estariam relacionados à contribuição das AC e à entrada de ACAS proveniente do giro subtropical. De qualquer forma, a CB permanece fortemente ligada à região de quebra de plataforma continental nas latitudes entre 24°S e 31°S, com uma porção significante do seu transporte em profundidades menores que 500 m. Isso tenderia a trazer resultados subestimados de transporte da CB baseados em cálculos geostróficos.

Based on hydrographic data, it is believed that the Malvinas Current has a strong barotropic component and that it is well-mixed (Peterson and Stramma 1991, Vivier and Provost 1999a).

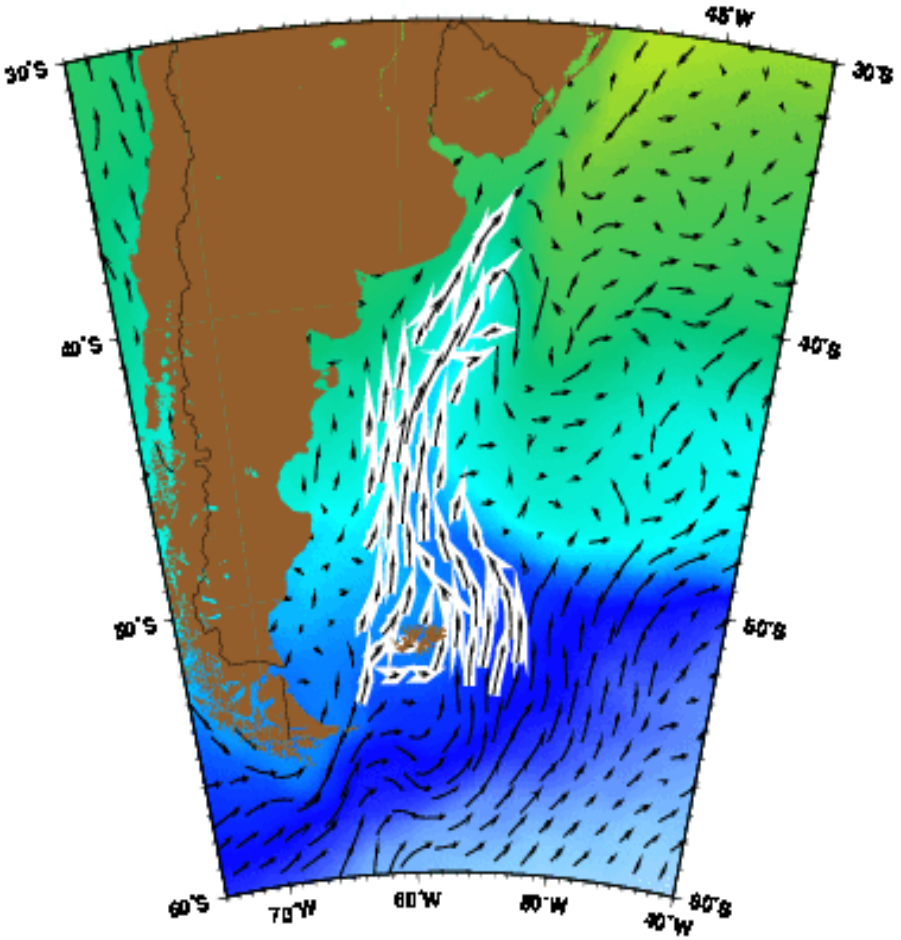

Estimates of the volume transport of the Malvinas Current vary widely in the literature, depending on the reference level that is chosen (Garzoli 1993). For example, using a reference level of 1000 m at 38°S, Garzoli (1993) obtained a transport of about 24 Sv.

Using a reference level of 1400 m at 42°S and 46°S, Gordon and Greengrove (1986) obtained values of 10 Sv at both locations, although they believed that this value represented the lower limit of the real flow. Piola and Bianchi (1990 as cited in Garzoli 1993), using 1000 m as the reference, found 10-12 Sv.

With a reference level of 3000 m at 42°S, Peterson (1992) found 60 Sv in the first 2000 m and 75 Sv in total, while at 46°S he found 70 Sv in the first 2000 m and 88 Sv in total.

http://oceancurrents.rsmas.miami.edu/atlantic/malvinas.html

Trayectoria de boya derivante

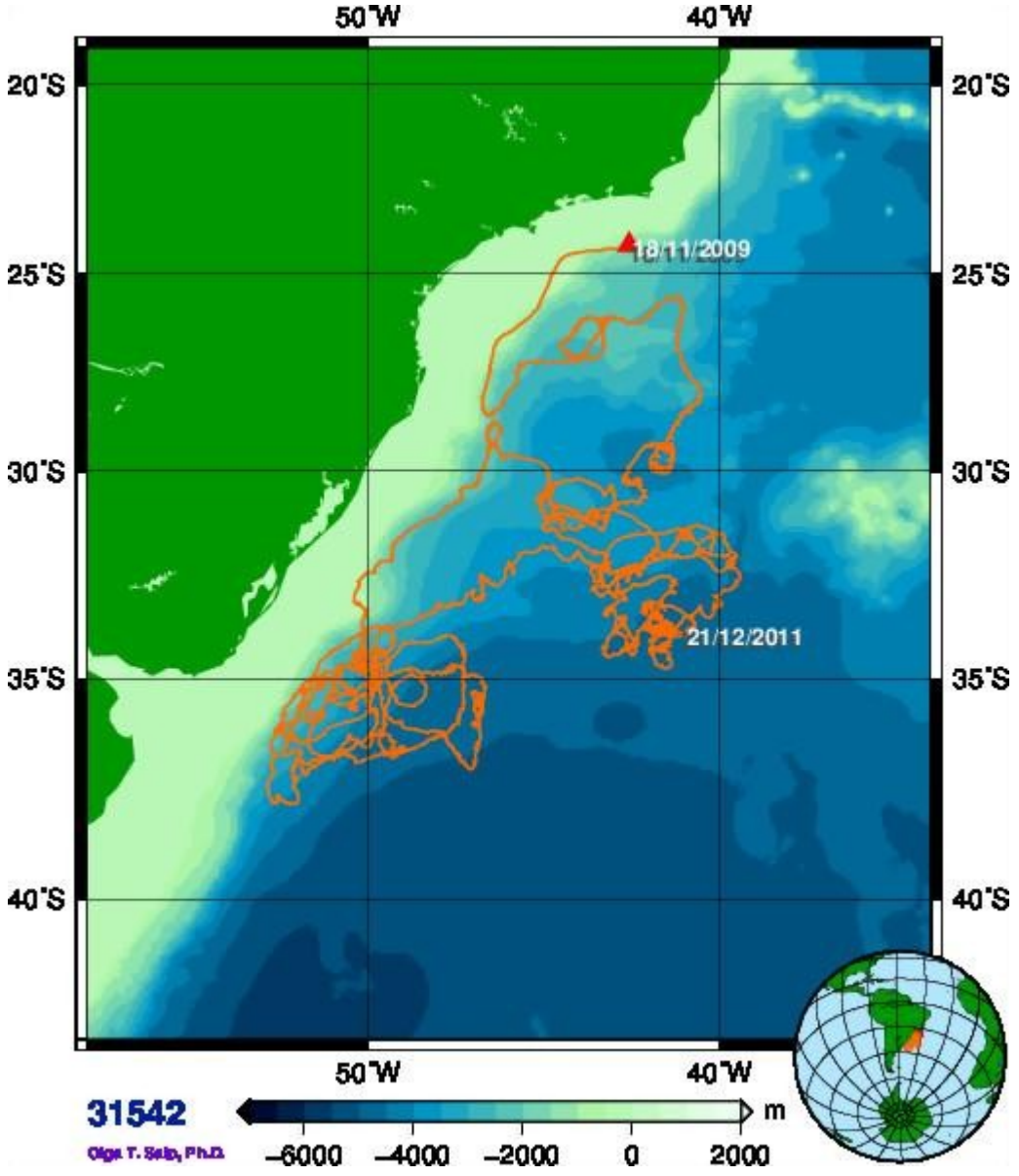

Variabilidad Oceanica de mesoescala

As instabilidades causadas pela interação entre as águas quentes da CB e as águas frias da CM na superfície produzem muitas feições de mesoescala, como meandros e vórtices. Segundo Garzoli e Simionato (1990), essas feições, somadas às instabilidades da CB e da CM, dominam a dinâmica da região da CBM. Para todo o oceano global, os vórtices são considerados estruturas fundamentais para a mistura de propriedades (sal, calor, momento, nutrientes etc.) na direção perpendicular às frentes oceanográficas. Conforme Baumgartner e Reichel (1975), na região da CBM existe um excesso de precipitação sobre evaporação, especialmente na região subantártica da frente entre a CB e a CM. Para essa região, a translação para sul de vórtices quentes oriundos da CB fornece sal e calor que contribuem para o balanço termoalino das águas subantárticas.

SEGUNDO Garcia et al. (2004), a maior parte dos vórtices da região da CBM são gerados por processos de retroflexão associados a reversos no sentido das correntes superficiais da área. Em sistemas como a corrente do Golfo e Kuroshio, por exemplo, o mecanismo predominante é o sistema clássico de meandramento causado por instabilidades zonais ao longo do eixo principal de direção da corrente. A orientação da costa na América do Sul é importante para a produção de vórtices a partir dos mecanismos de retroflexão da CB e da CM na região da CBM.

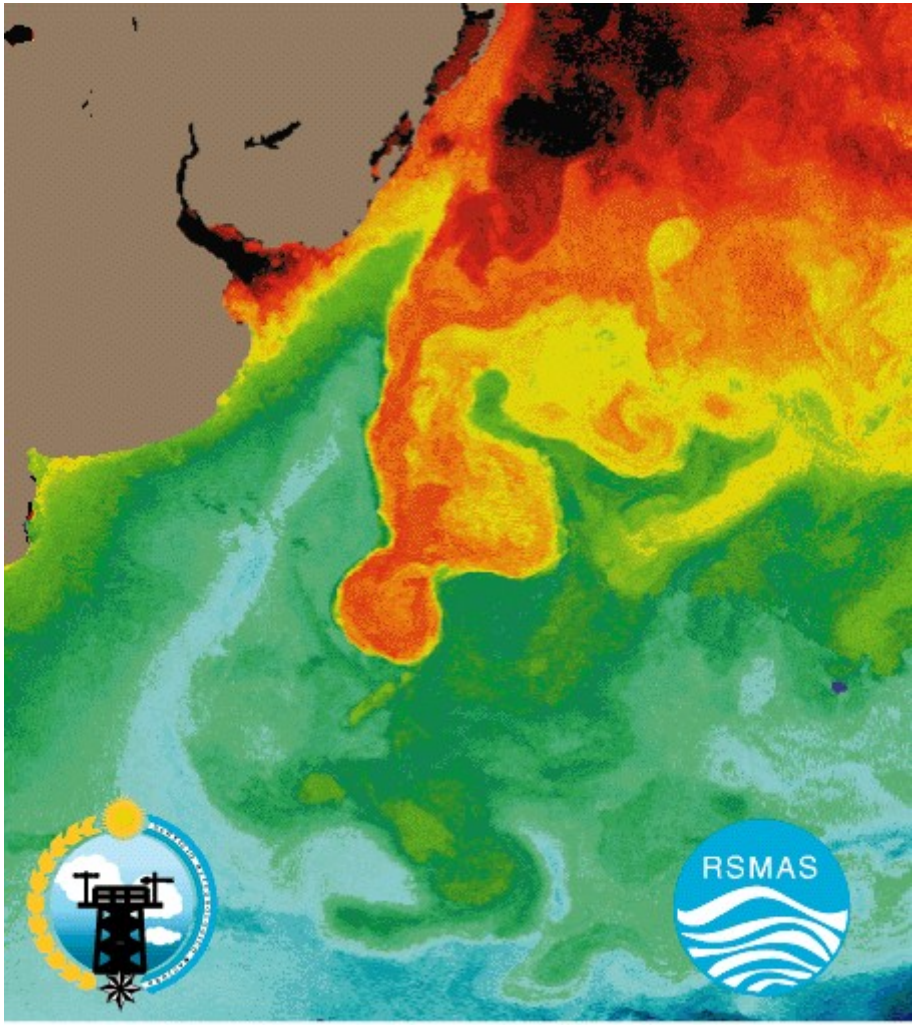

Figure 14. SST mosaic for 1-5 November 1988 that exhibits the formation of a warm-core eddy from the Brazil current.

LENTINI, Olson e Podestá (2002) utilizaram dados de seis anos de imagens de satélite para descrever os vórtices quentes e frios da região da CBM entre 1993 e 1998. Segundo os autores, pelo menos sete vórtices quentes são ejetados da CB por ano, sobretudo nos meses de primavera e verão, quando a posição da retroflexão da CB está mais para sul. Eles reconhecem, no entanto, que durante o inverno e o outono, muita informação é perdida pela intensa cobertura de nuvens na região da CBM.

Energía cinética de eddies de mesoescala

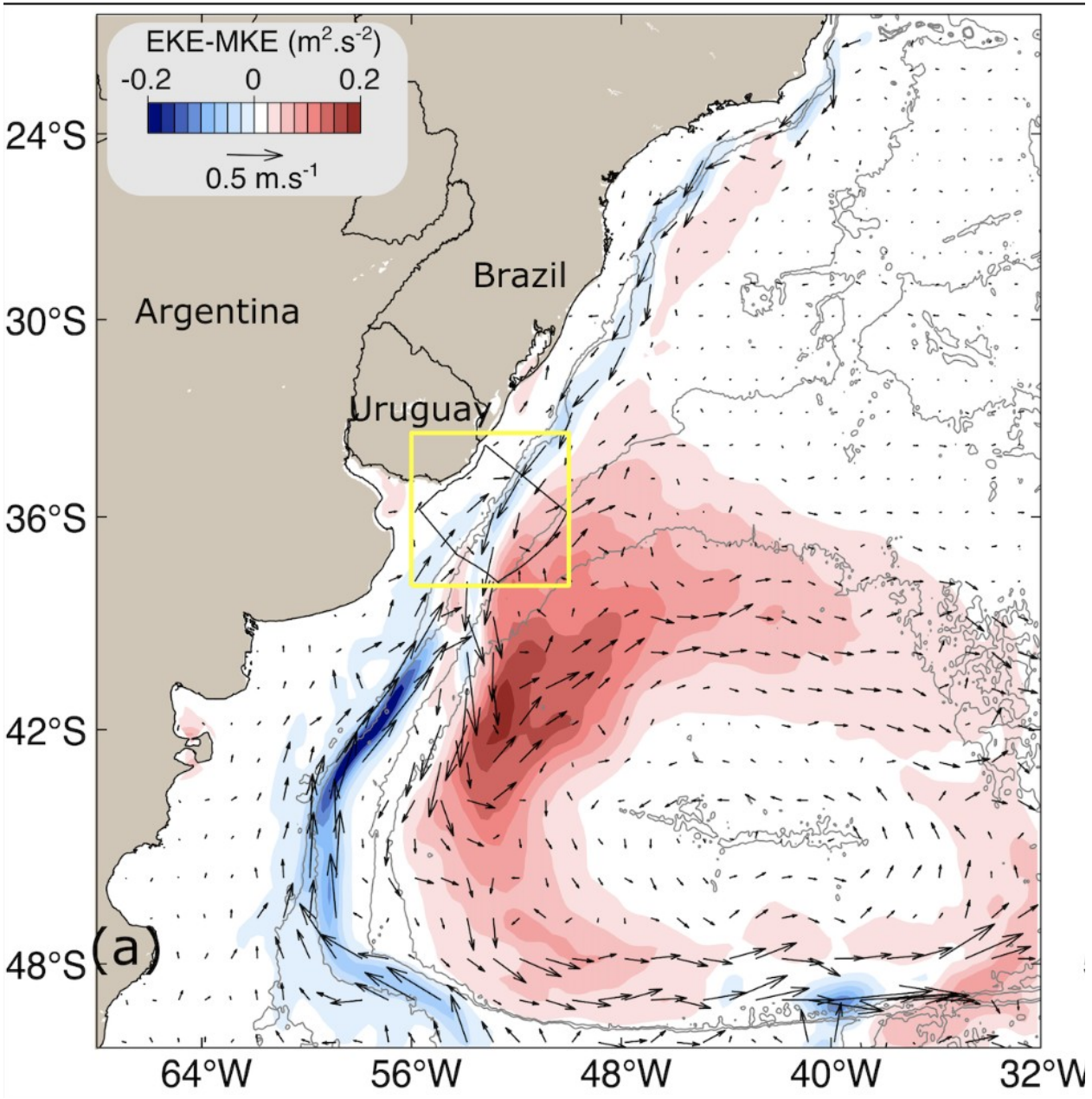

Manta et al 2024

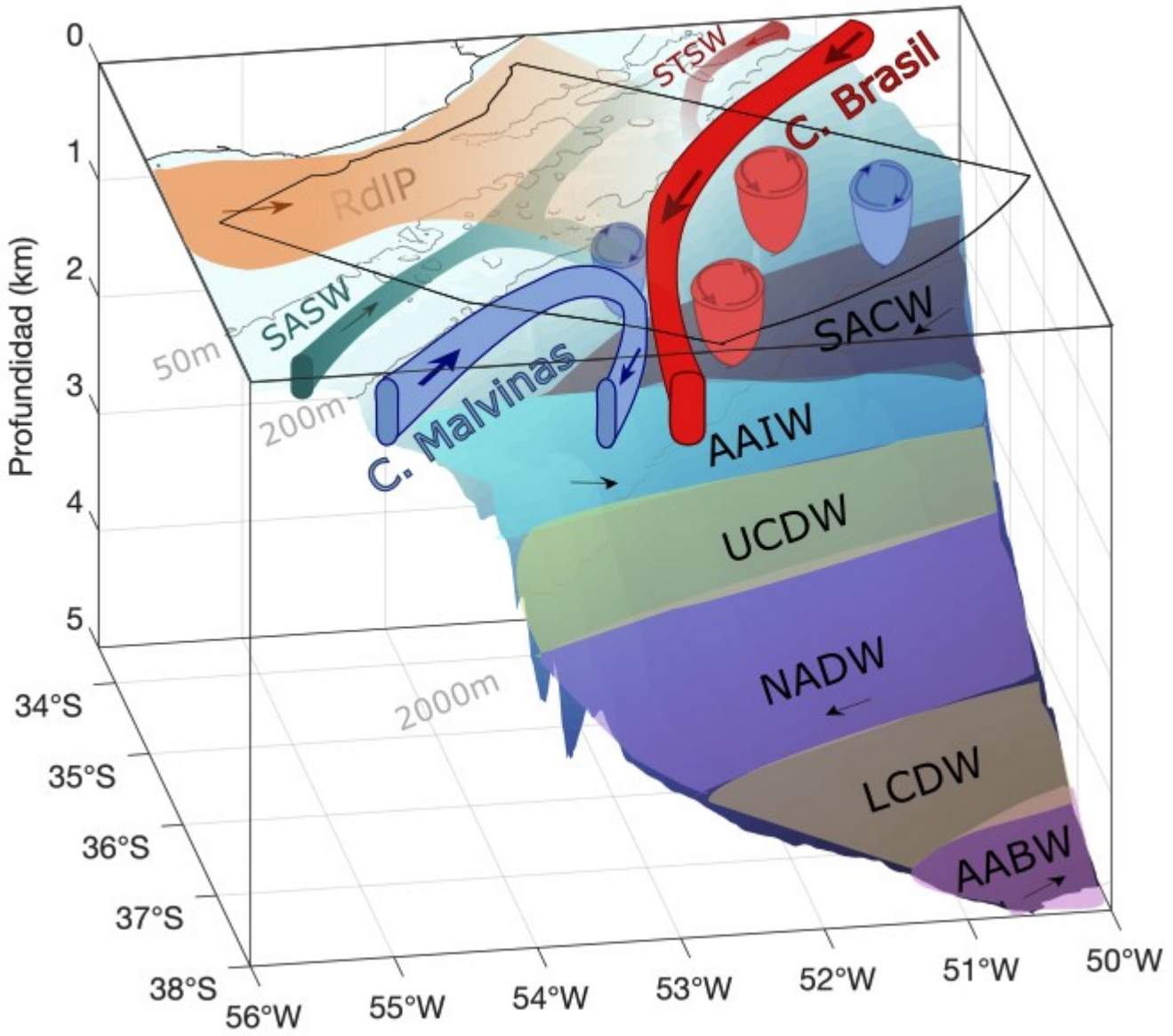

Manta et al 2024

Modos de Variabilidad del Atlantico Sur

AGCM+simple ocean models

1) Passive mixed layer

The first model in the hierarchy is a passive mixed layer model for which the equation of the mixed layer temperature T is given by

$$\frac{\partial T}{\partial t} = -\frac{Q}{h\rho_w c_p} + F_m. \qquad (1)$$

Here Q is the net surface heat flux leaving the ocean, h the mixed layer depth, ρ_w the density, c_p the specific heat capacity of seawater, and F_m represents the induced heat transport by the ocean and all other processes neglected by (1). To ensure that the climatology of the mixed layer model stays close to the observed climatology, we computed F_m using (1) from a 50-yr atmosphere-only run with prescribed SSTs:

$$F_m = \frac{\partial T_{\text{clim}}}{\partial t} + \frac{Q_{\text{diag}}}{h\rho_w c_p}, \qquad (2)$$

where T_{clim} is the daily mean observed climatological SST computed by linear interpolation from the climatological monthly mean SST of Da Silva et al. (1994),

Dipolo del Atlantic Sur (SAD)

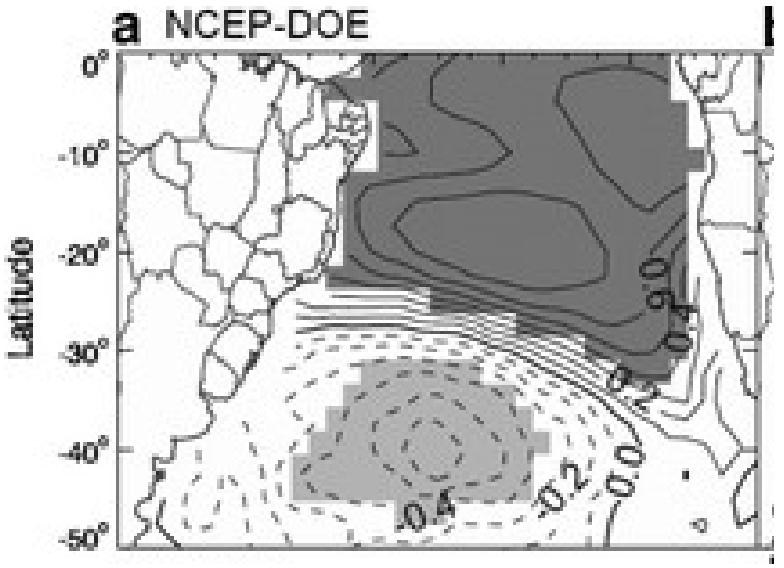

Haarsma et al 2005

2) Mixed layer dynamics

Including advection and wind-induced mixing, the equation for the mixed layer becomes

$$\frac{\partial T}{\partial t} = -\frac{1}{h}\left(\frac{Q}{\rho_w c_p} + \mathbf{U}\cdot\nabla_h T + w\Delta T\right) + W + F_r, \quad (3)$$

where $\mathbf{U}$ is the horizontal transport in the mixed layer, ∇_h is the horizontal part of the gradient operator, and w and ΔT are the vertical velocity and temperature jump at the base of the mixed layer; W is the temperature tendency in the mixed layer due to wind-induced mixing and F_r represents, similar as F_m in (1), all the processes neglected by (3). The advection terms we are considering in this article are Ekman and barotropic transport; that is, $\mathbf{U} = \mathbf{U}_e + \mathbf{U}_b$.

potentially an important process. Based on the mixed layer model of Niiler and Kraus (1977), SH estimates the effect of wind-induced mixing on SST to be proportional to the cube of the friction velocity divided by the mixed layer depth,

$$W = -\frac{\alpha}{h}u_*^3, \quad (7)$$

The vertically integrated horizontal Ekman velocity or Ekman transport $\mathbf{U}_e$ is given by

$$\mathbf{U}_e = (U_e, V_e) = \frac{1}{\rho_w(f^2 + r^2)}(f\tau_y + r\tau_x, -f\tau_x + r\tau_y), \quad (4)$$

where f is the Coriolis parameter, τ the wind stress, and r a linear friction term. For $r = 0$, the usual form of Ekman transport is retrieved. Requiring the Ekman transport to be divergence free yields the vertical or Ekman pumping velocity:

$$w_e = \nabla_h \cdot \mathbf{U}_e = \frac{1}{\rho_w(f^2 + r^2)}[f(\nabla \times \boldsymbol{\tau})_z + r\nabla\cdot\boldsymbol{\tau}]. \quad (5)$$

The barotropic transport in the mixed layer $\mathbf{U}_b$ is estimated by solving the Stommel equation for a wind-driven barotropic flow:

$$\kappa_s\nabla^2\psi + \frac{\partial_\phi f}{a^2\cos\phi}\frac{\partial\psi}{\partial\lambda} = \frac{\mathbf{k}\cdot\nabla\times\boldsymbol{\tau}}{\rho_o}, \quad (6)$$

where ψ is the barotropic streamfunction, ϕ latitude, λ longitude, a the radius of the earth, $\mathbf{k}$ the unit vector in the vertical, and κ_s is the linear friction coefficient. When discretized this equation gives a linear set of equations $A\psi = b$, which is solved using a lower upper (LU) decomposition of A. To obtain the barotropic transport in the mixed layer (U_b), the barotropic velocity $\boldsymbol{u}_b$, derived from ψ, is multiplied by the mixed layer depth h.

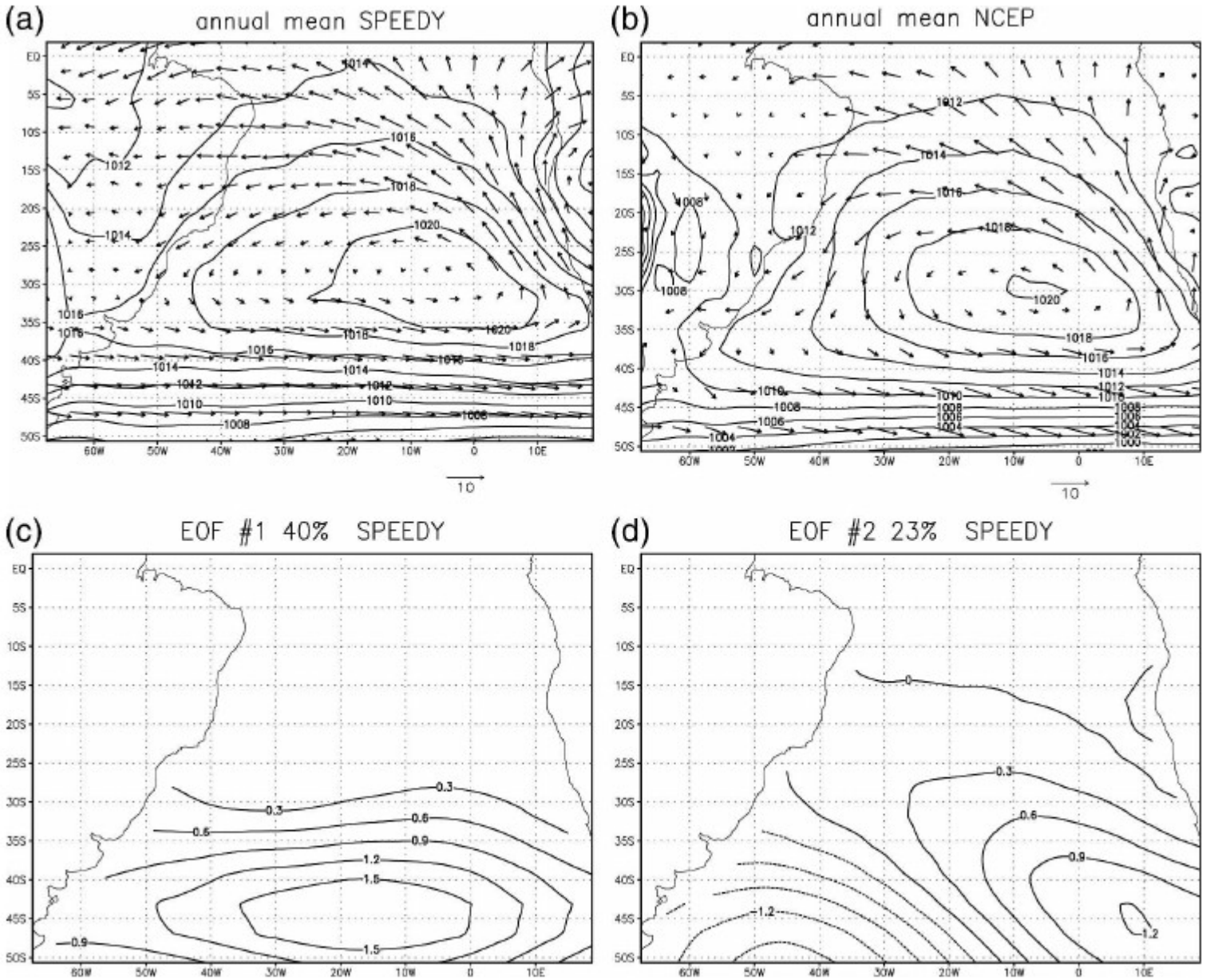

FIG. 1. Annual mean MSLP (hPa) and near-surface winds (m s^{-1}) (a) simulated by SPEEDY with prescribed climatological SSTs and (b) obtained from the NCEP–NCAR reanalysis. (c), (d) The first two EOFs of MSLP simulated by SPEEDY for 3-month seasonal mean averages from which the annual cycle is subtracted.

SVD1 – AGCM+Full ocean model

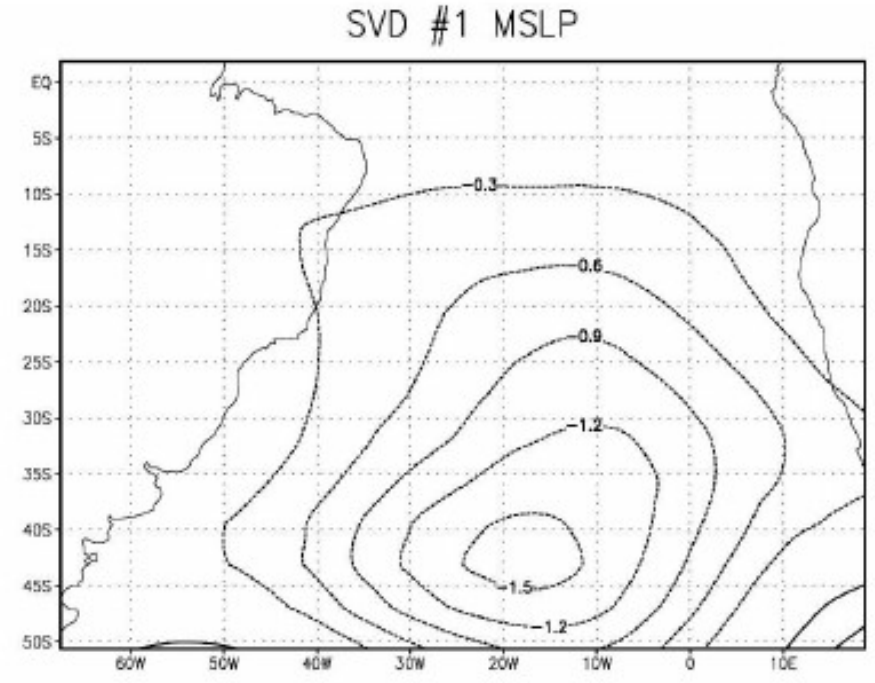

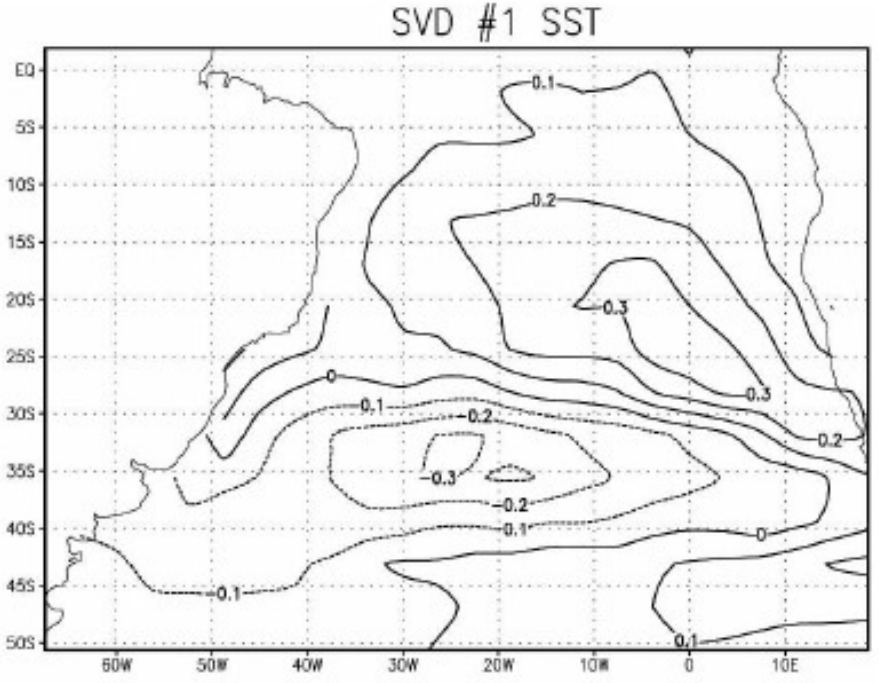

SVD1 - AGCM+slab

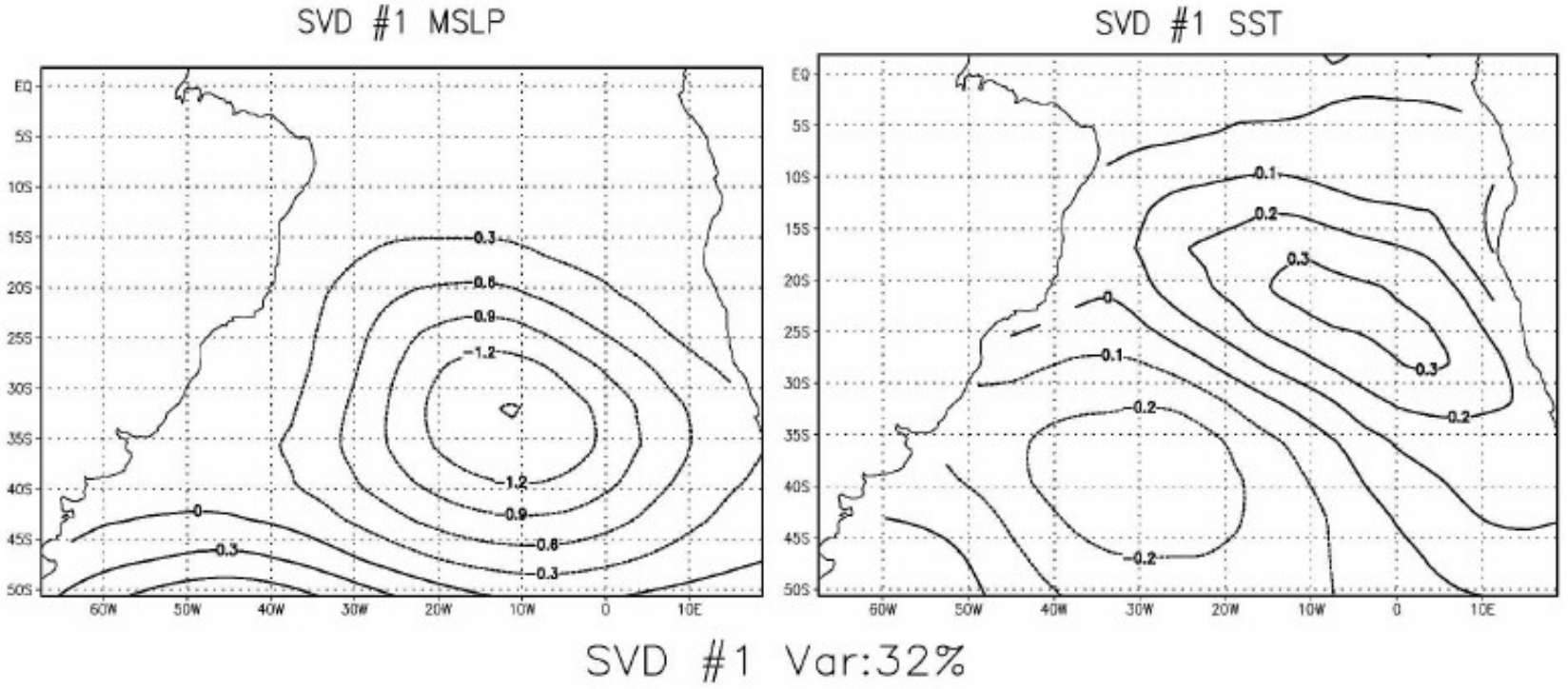

FIG. 3. The leading mode of a combined SVD analysis of MSLP (hPa) and SST (K) anomalies for the SPEEDY-passive mixed layer run. The spatial patterns are scaled such that the values correspond to one standard deviation. The explained total squared variance is 32%.

duces anomalous meridional advection. From this we conclude that the equatorward pole of the SST dipole is caused by enhancement or decrease of the climatological trade winds, which consequently enhance or diminish the latent heat flux, whereas the poleward pole is caused by anomalous meridional advection of climatological surface air temperatures (SATs).

SVD1 – AGCM+slab+Ekman transport+wind mixing

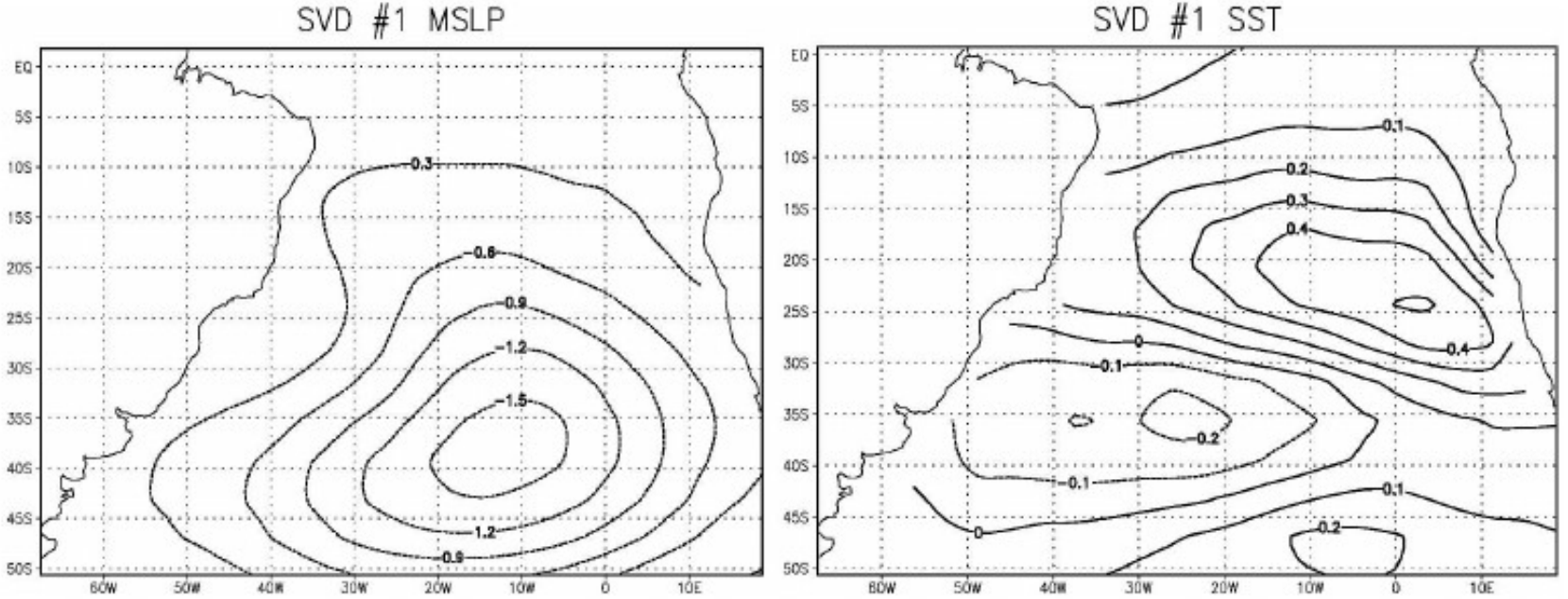

FIG. 4. As in Fig. 2 but for the run with Ekman transport and wind-induced mixing with a variable mixed layer depth.

tably, the southern pole of the SST dipole pattern shows a much more elongated structure in agreement with the fully coupled model and observations. However, the amplitude of this poleward pole seems to be overestimated, whereas the amplitude of the equatorward pole is reduced and is smaller than simulated by SPEEDY–MICOM. A regression analysis between the the anomalous meridional advection of climatological SST by anomalous meridional Ekman velocity caused by anomalous zonal winds. Anomalous winds and climatological SST gradients are strongest in the southern part of the basin, explaining the dominance of the Ekman transport term there. Comparison between the

$$\frac{\partial T}{\partial t} = -\frac{1}{h}\left(\frac{Q}{\rho_w c_p} + \hat{\mathbf{U}} \cdot \nabla_h T + \hat{w}\Delta T + \alpha \hat{u}_*^3\right) + F'_r, \qquad (8)$$

Comparing the three terms in Fig. 5 we see that for the equatorward pole the surface flux is the dominant term except for the southeastern corner, whereas for the poleward pole all three terms seem to be important for the correct simulation. There appears to be a partial cancellation between the Ekman transport and the wind-induced mixing terms.

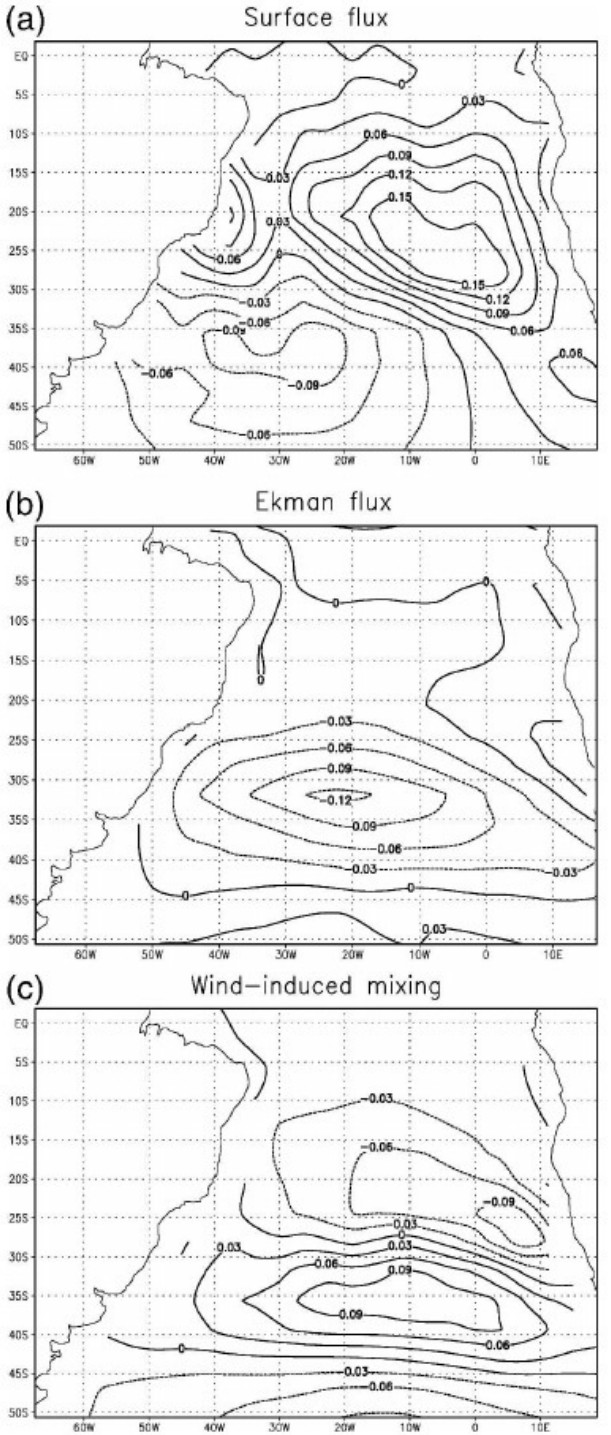

FIG. 5. Regression of the PC of MSLP of the first MSLP–SST SVD mode onto the different terms in the tendency equation: (a) surface flux, (b) Ekman transport, and (c) wind-induced mixing. The units are in kelvin (3 month)$^{-1}$.

Role of barotropic transport important only in strong boundary currents.

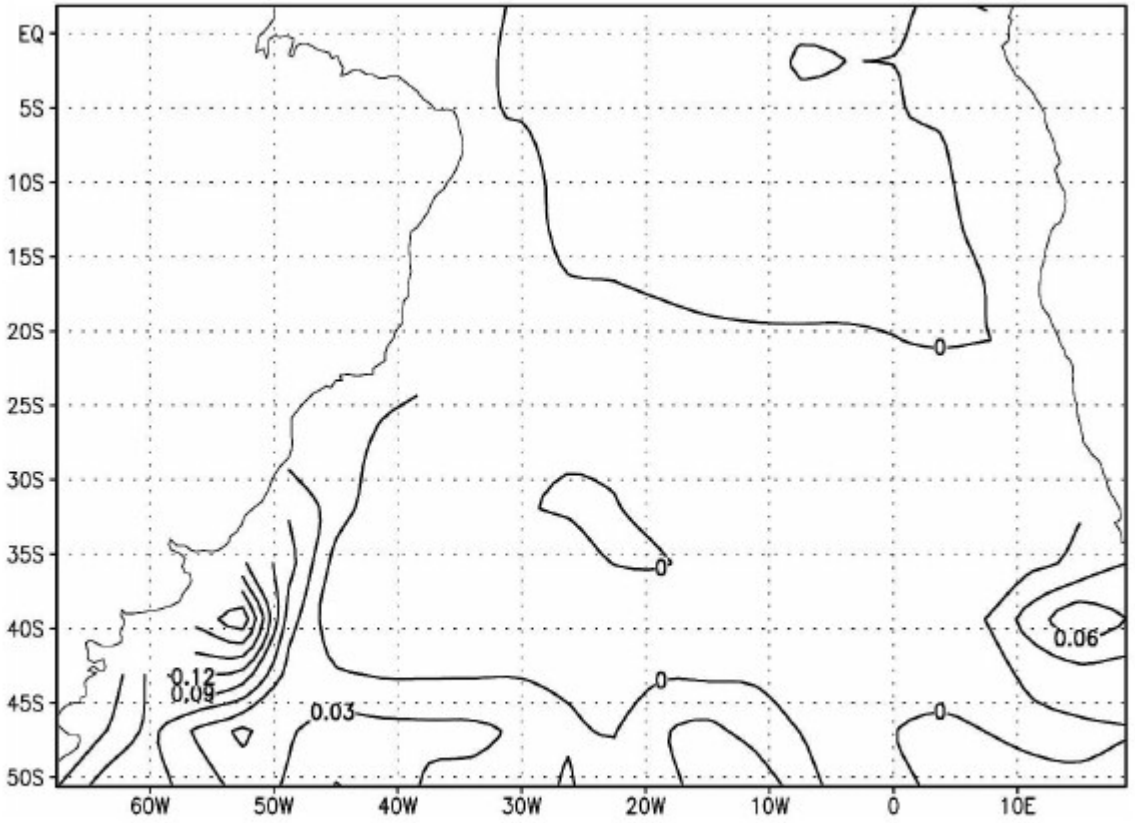

FIG. 6. Regression of the PC of the first EOF mode of MSLP onto the barotropic transport term in the tendency equation (8) for the SST. The units are in kelvin (3 month)$^{-1}$.

Malvinas confluence zone. In the Brazil–Malvinas confluence zone large SST gradients exist. Small changes in the in the boundary currents due to anomalous wind forcing can therefore easily generate large SST anomalies. A sensitivity analysis of SST variability due to the

Heat Budget

$$\frac{\partial T}{\partial t} = -\frac{1}{h}\left(\frac{Q}{\rho_w c_p} + \hat{\mathbf{U}} \cdot \nabla_h T + \hat{w}\Delta T + \alpha \hat{u}_*^3\right) + F'_r, \qquad (8)$$

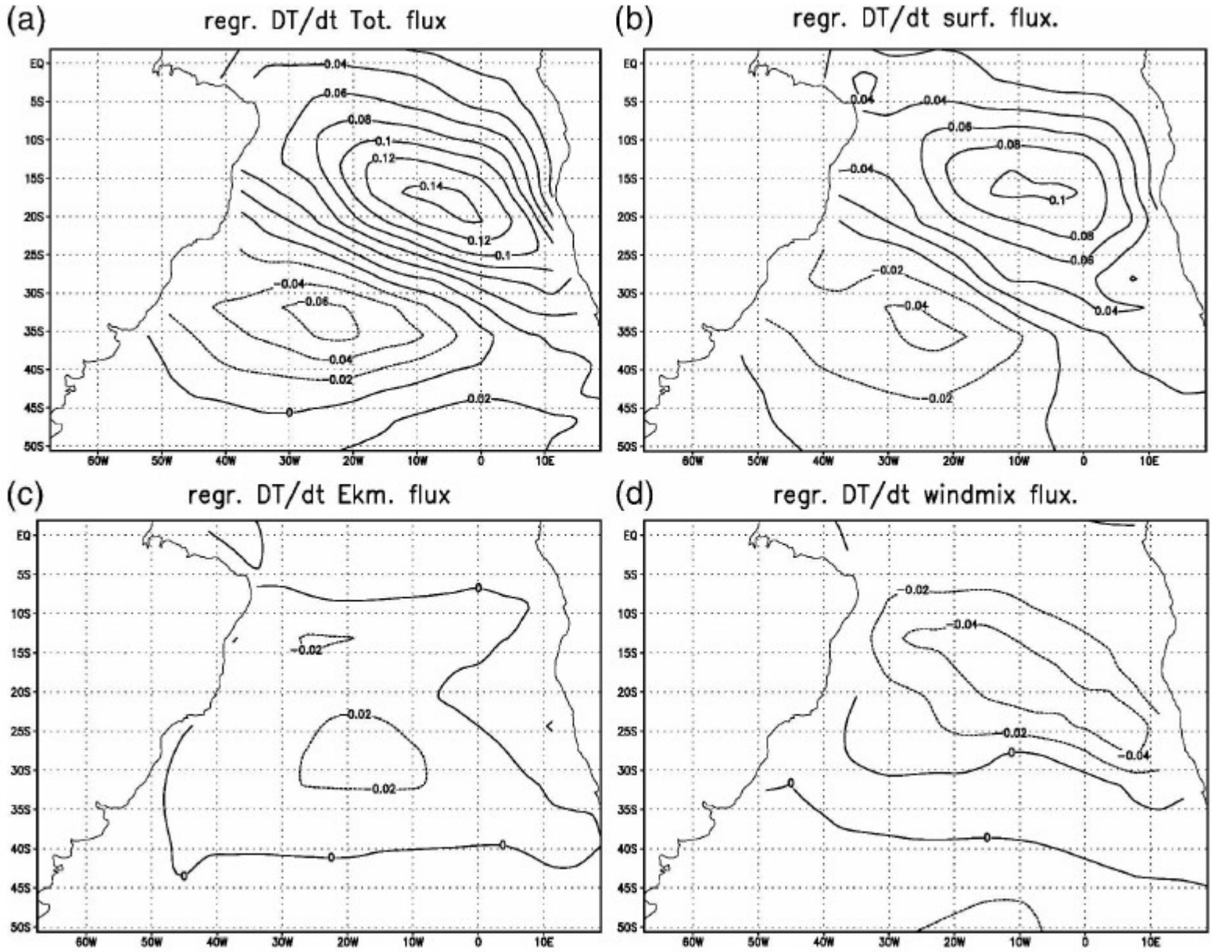

FIG. 7. Regression of the SST tendency onto the different terms in the tendency equation: (a) total heat flux, (b) surface flux, (c) Ekman transport, and (d) wind-induced mixing. The units are in kelvin (3 month)$^{-1}$.

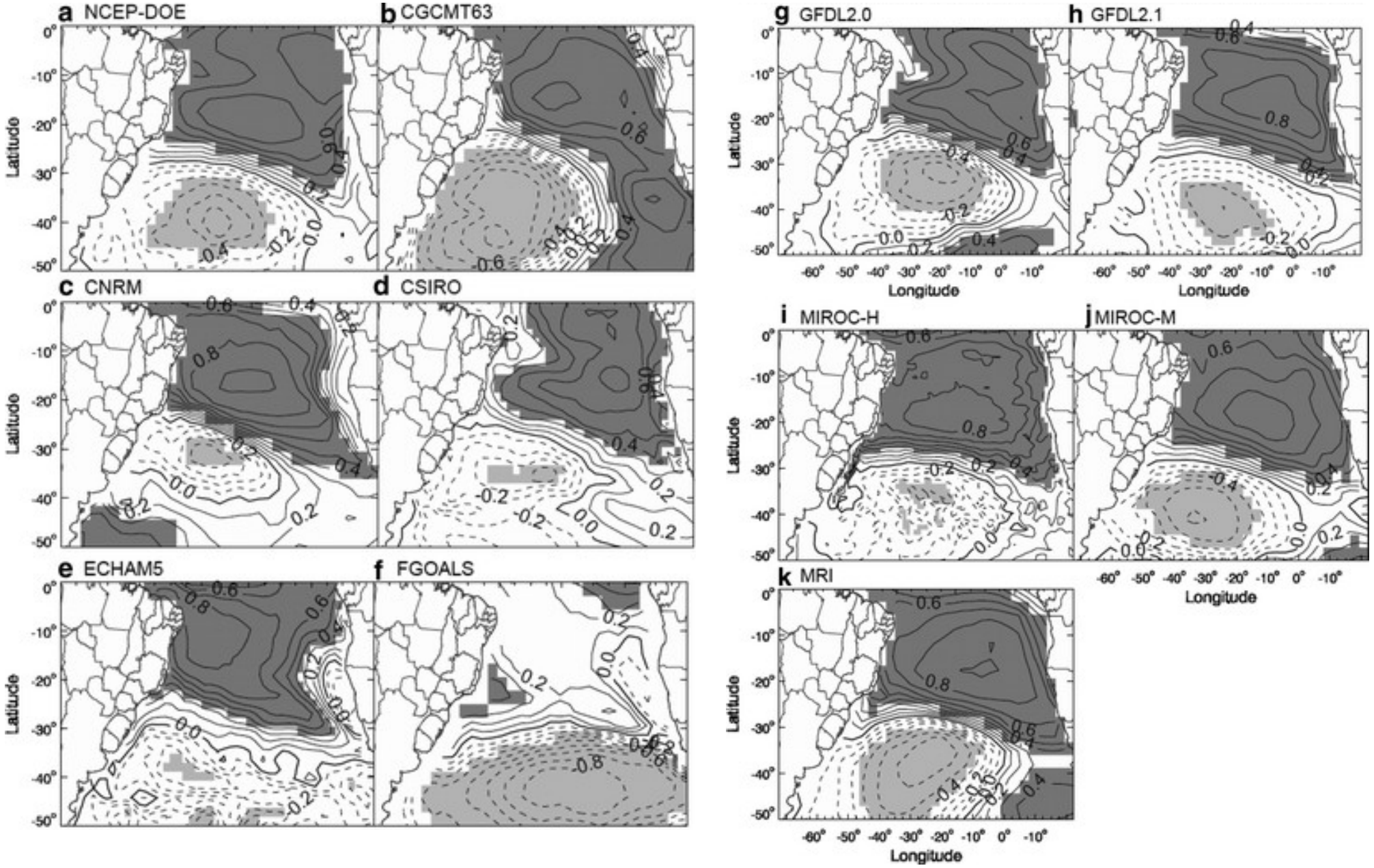

SAD in CMIP3 coupled models

Bombardi et al 2011

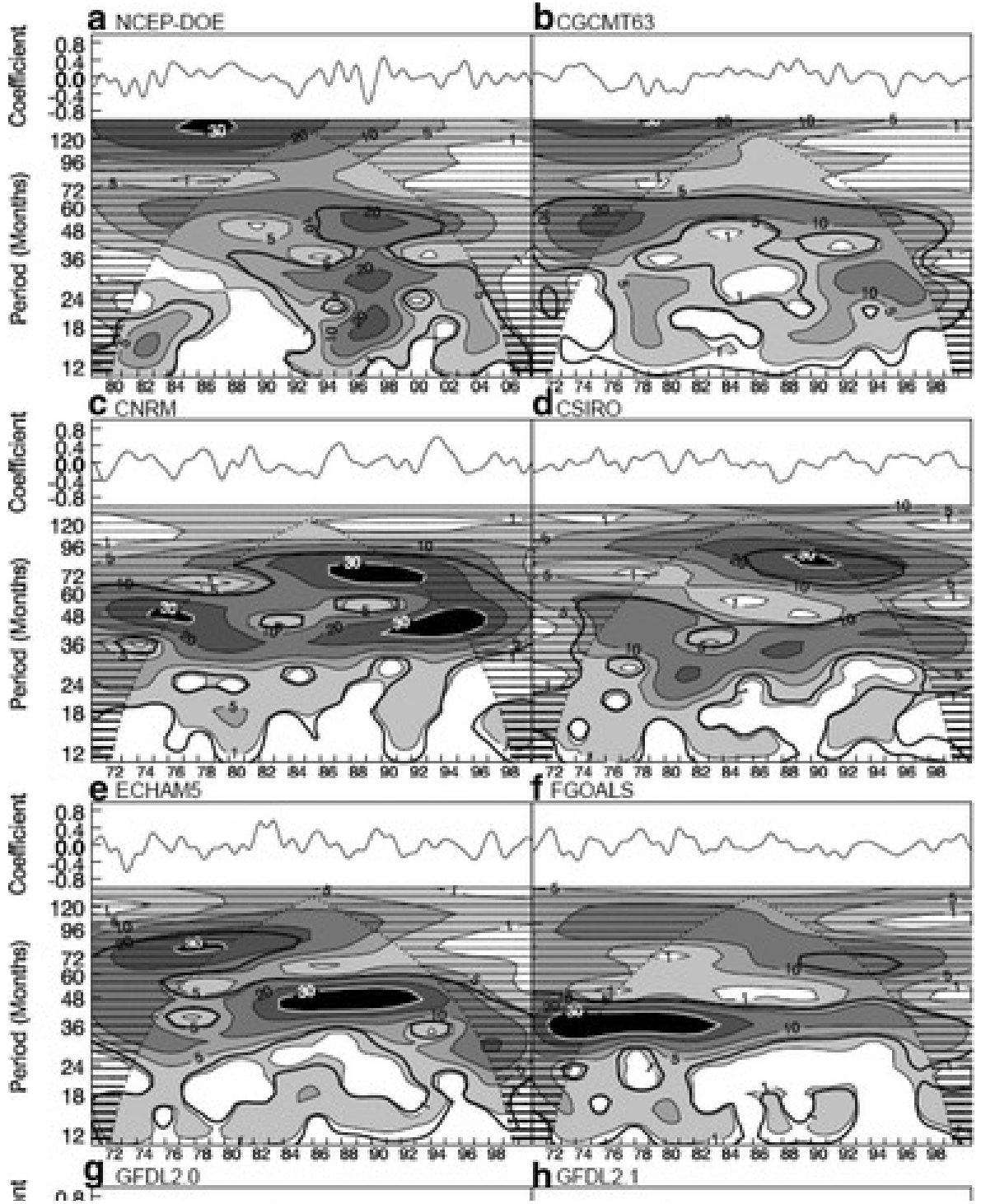

Bombardi et al 2011

Reconstructed SAD index last 12000 years

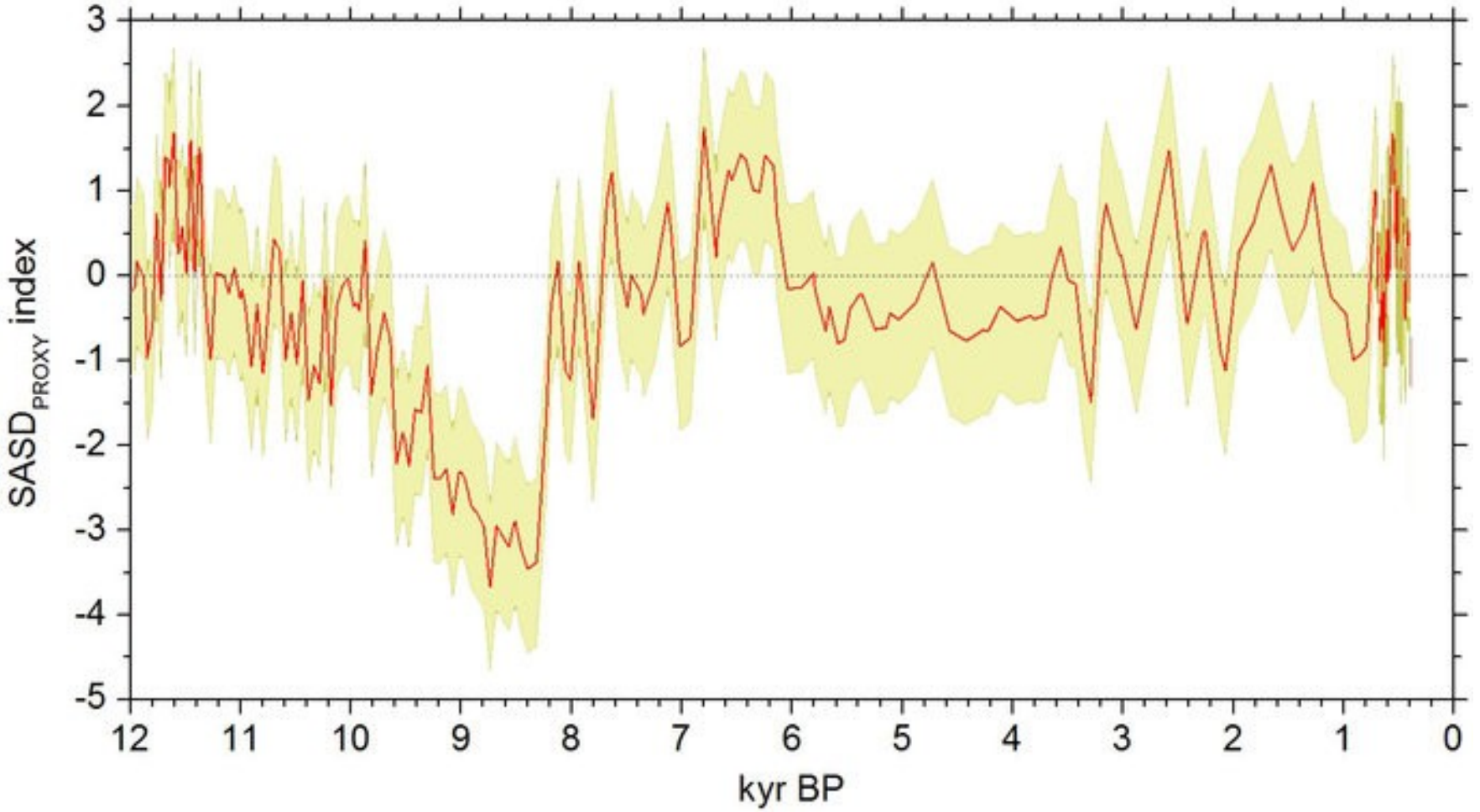

Wainer et al 2014

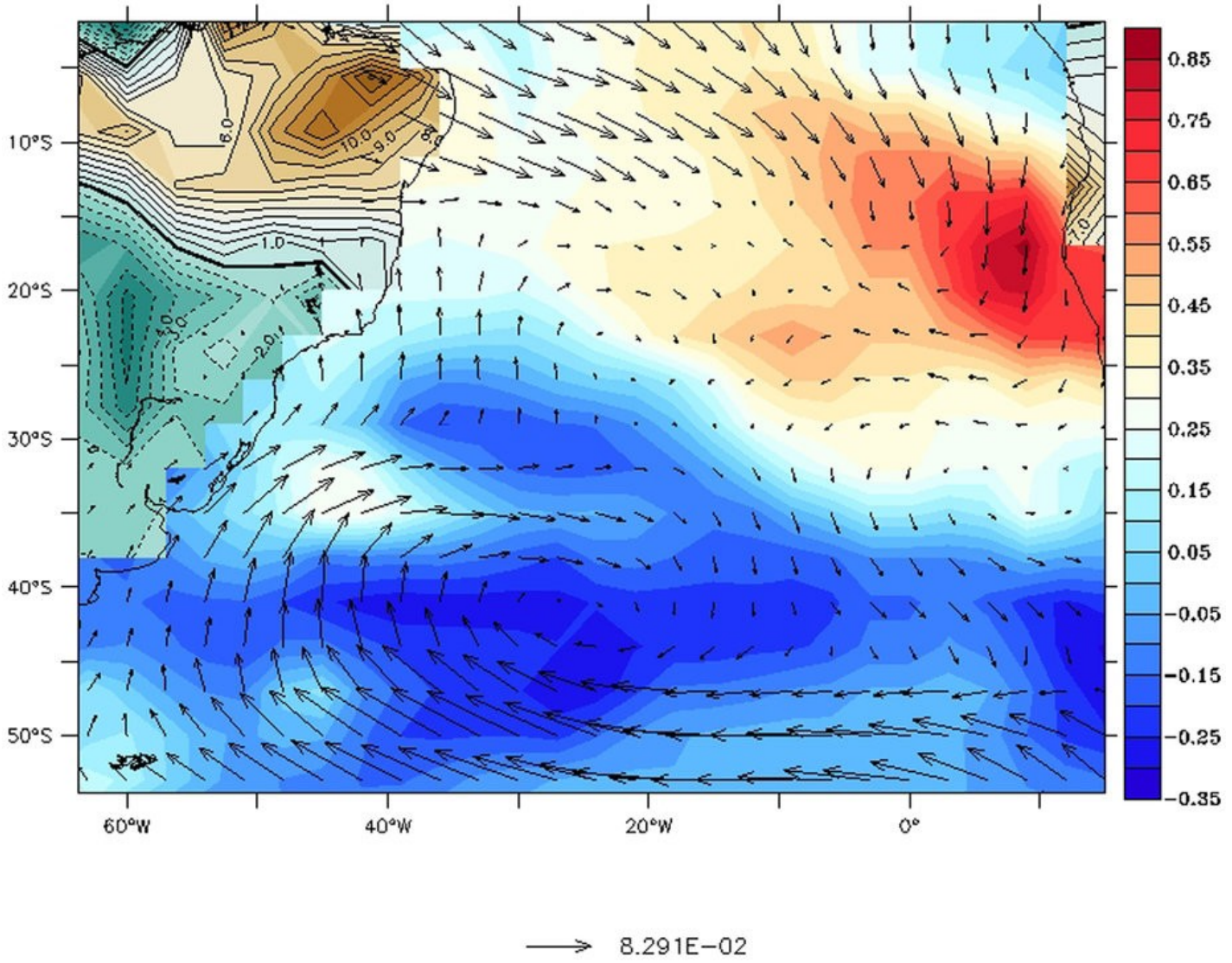

SST (°C, color shading over the ocean), wind-stress (dyne/cm2, vectors) and continental precipitation (brown and green shading with positive and negative black contours overlaid, mm/day). The SASD dipole, which is the dominant pattern of SST for the South Atlantic, emerges from the composite differences (in its negative phase) with negative differences in the Southwestern Pole and positive ones in the Northeastern Pole. The precipitation composite difference also shows a dipole pattern over South America. It displays wetter conditions (positive contours) for northern South America and drier conditions (negative contours) to the south. The composite differences in the wind-stress circulation strongly point the role of the South Atlantic in providing moisture for the wet Northeastern Brazil. Figure created with Ferret software.

The South Atlantic Dipole via Multichannel Singular Spectrum Analysis

Gaston Manta[1,2,3*], Eviatar Bach[1,4*], Stefanie Talento[5], Marcelo Barreiro[2], Sabrina Speich[1], and Michael Ghil[1,6,7]

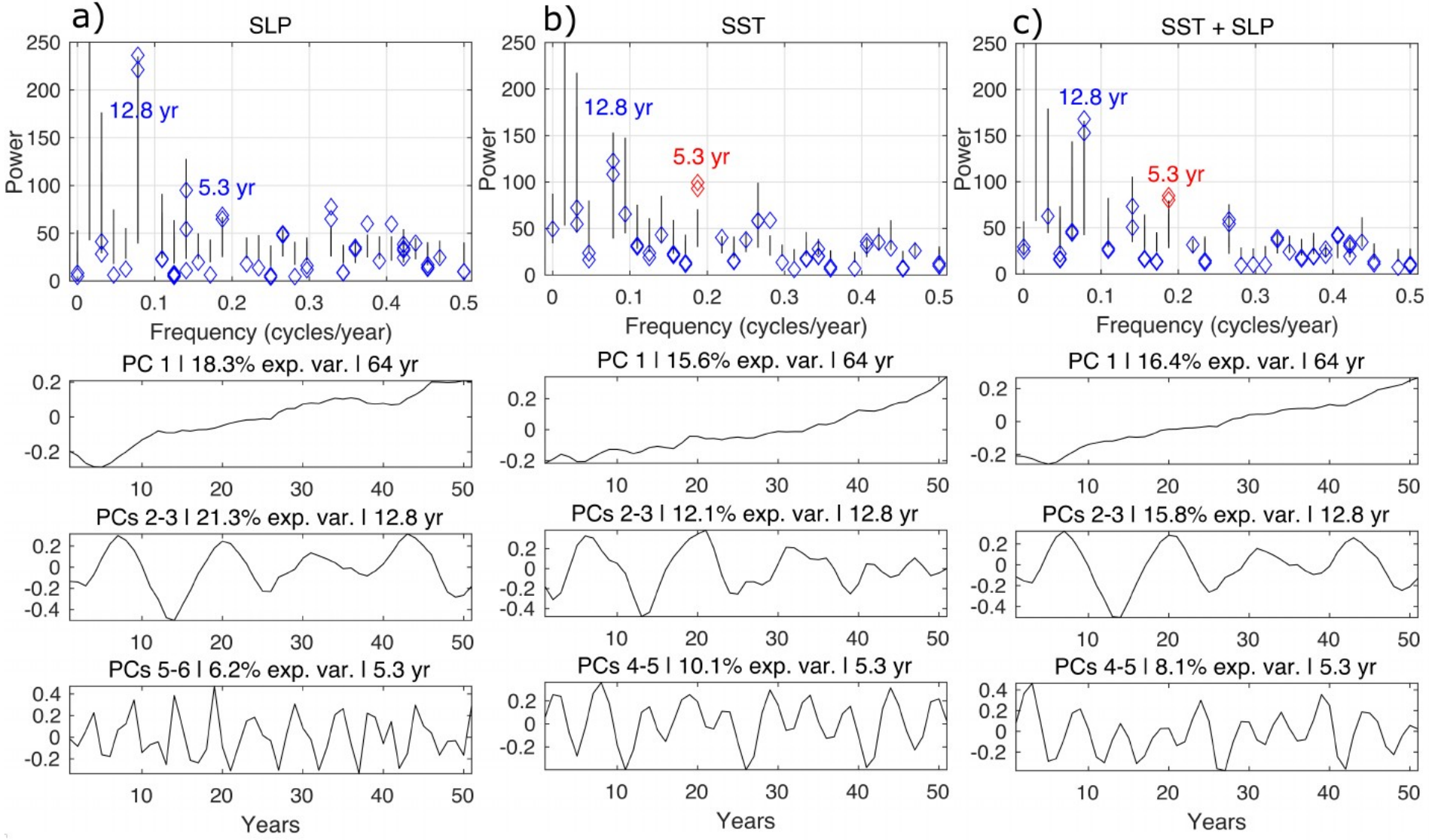

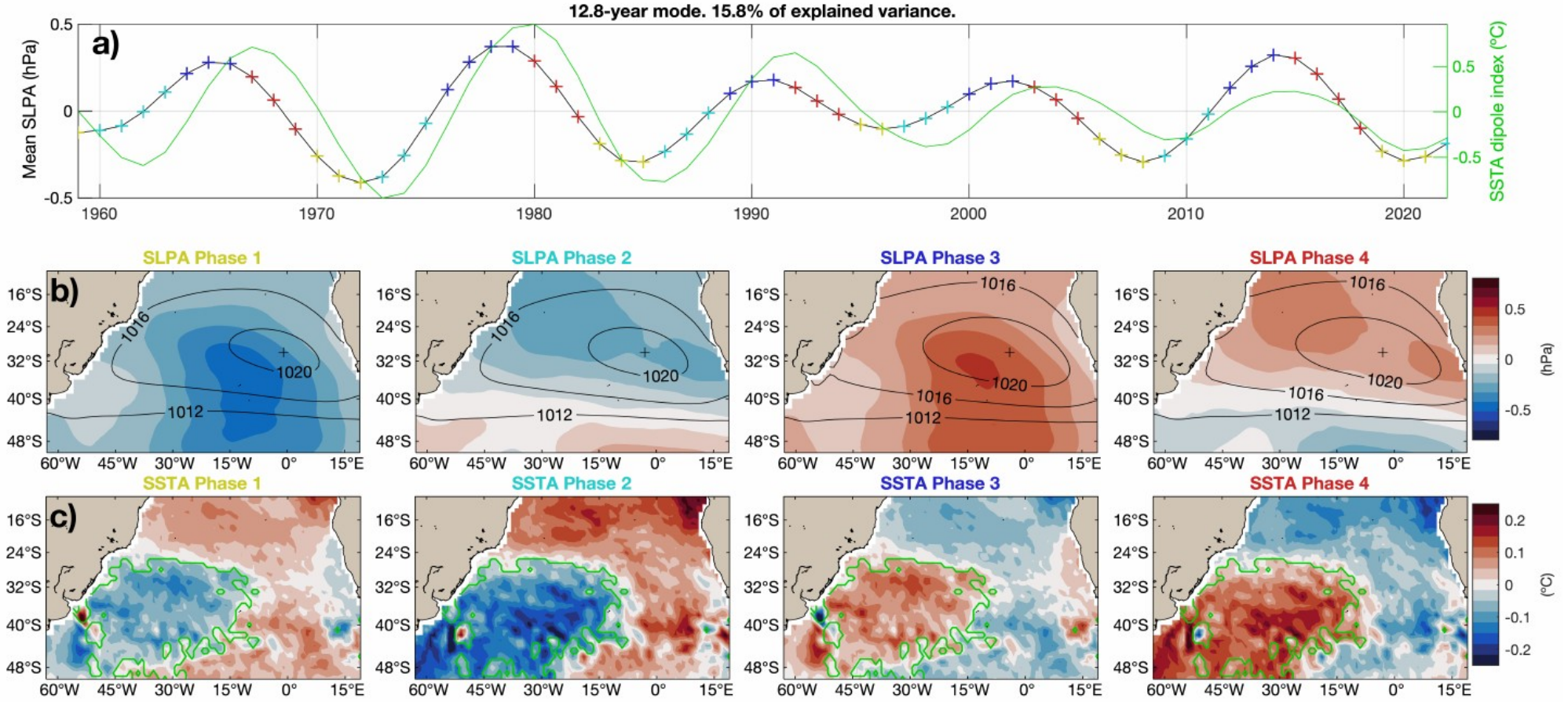

Figure 4. Reconstructed 12.8-year oscillatory coupled mode. a) Spatially averaged SLPAs in the domain. The line with colored plus signs shows the four phases of the mode, which are plotted in b) for the SLPAs and in c) for the SSTAs, while the solid green line shows the dipole index. A solid green line also separates the two cluster regions in SSTAs that are used to compute the dipole index. Both b) and c) also show in contours the mean SLP field plus the anomalies associated to the mode. Note that for plotting the contours of SLP, the anomalies were multiplied by 3 before adding the mean flow, to better appreciate the differences between the phases.

Manta et al 2024

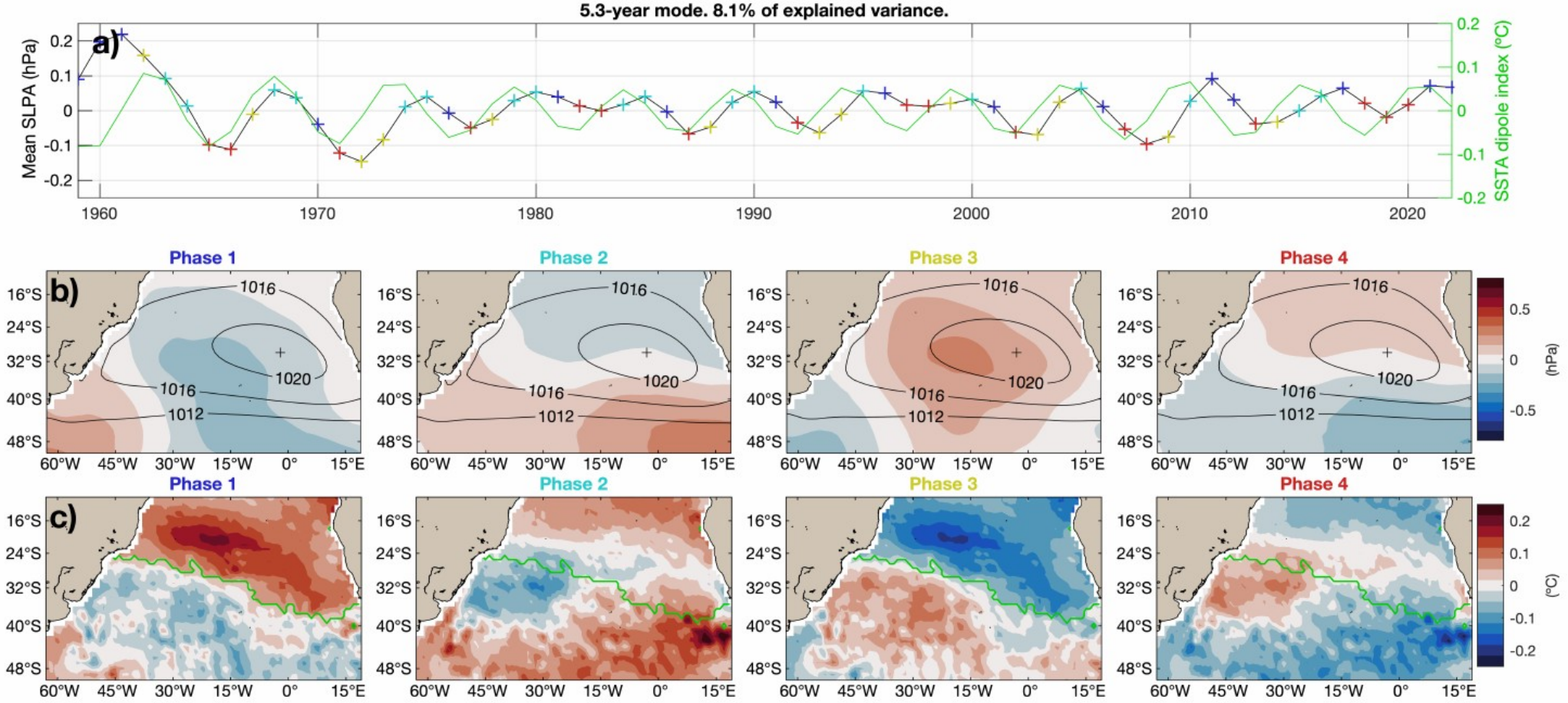

Figure 5. Reconstructed 5.3-year oscillatory coupled mode. a) Spatially averaged SLPAs in the domain. The line with colored plus signs shows the four phases of the mode, which are plotted in b) for the SLPAs and in c) for the SSTAs, while the solid green line shows the dipole index. Green lines in each of the four plots of panel c) separate the two cluster regions used to compute the dipole index. Both b) and c) also show in contours the mean SLP field plus the anomalies associated with the mode. As in Figure 4, the SLPAs were multiplied by 3 before adding the mean flow, to better appreciate the differences between the phases.

Manta et al 2024

Modos de Variabilidad en el Atlantico Tropical

Atlantic dipole
Gradient Mode

MAM

Atlantic Niño
Zonal Mode

JJA

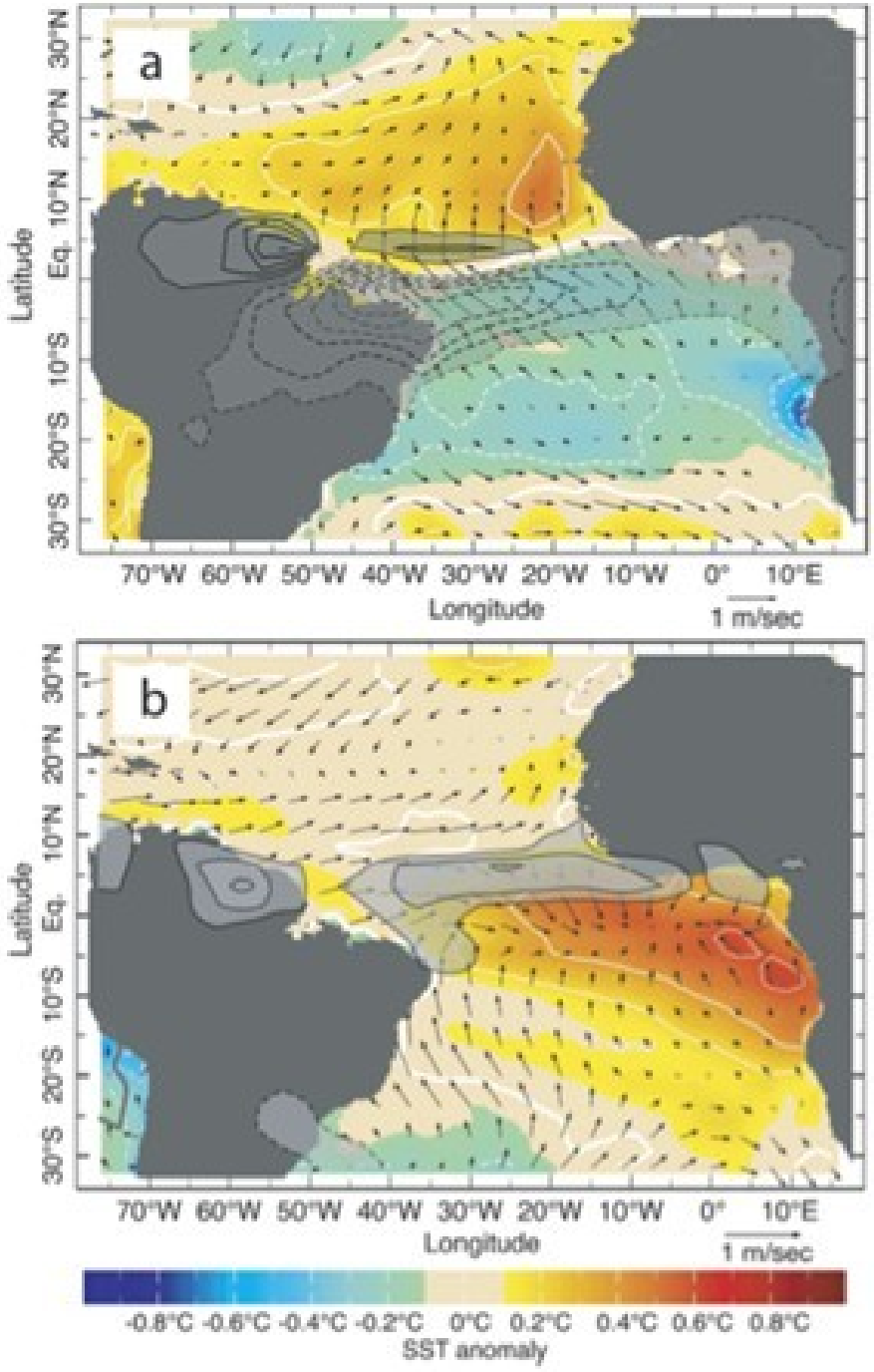

Kushnir et al 2006

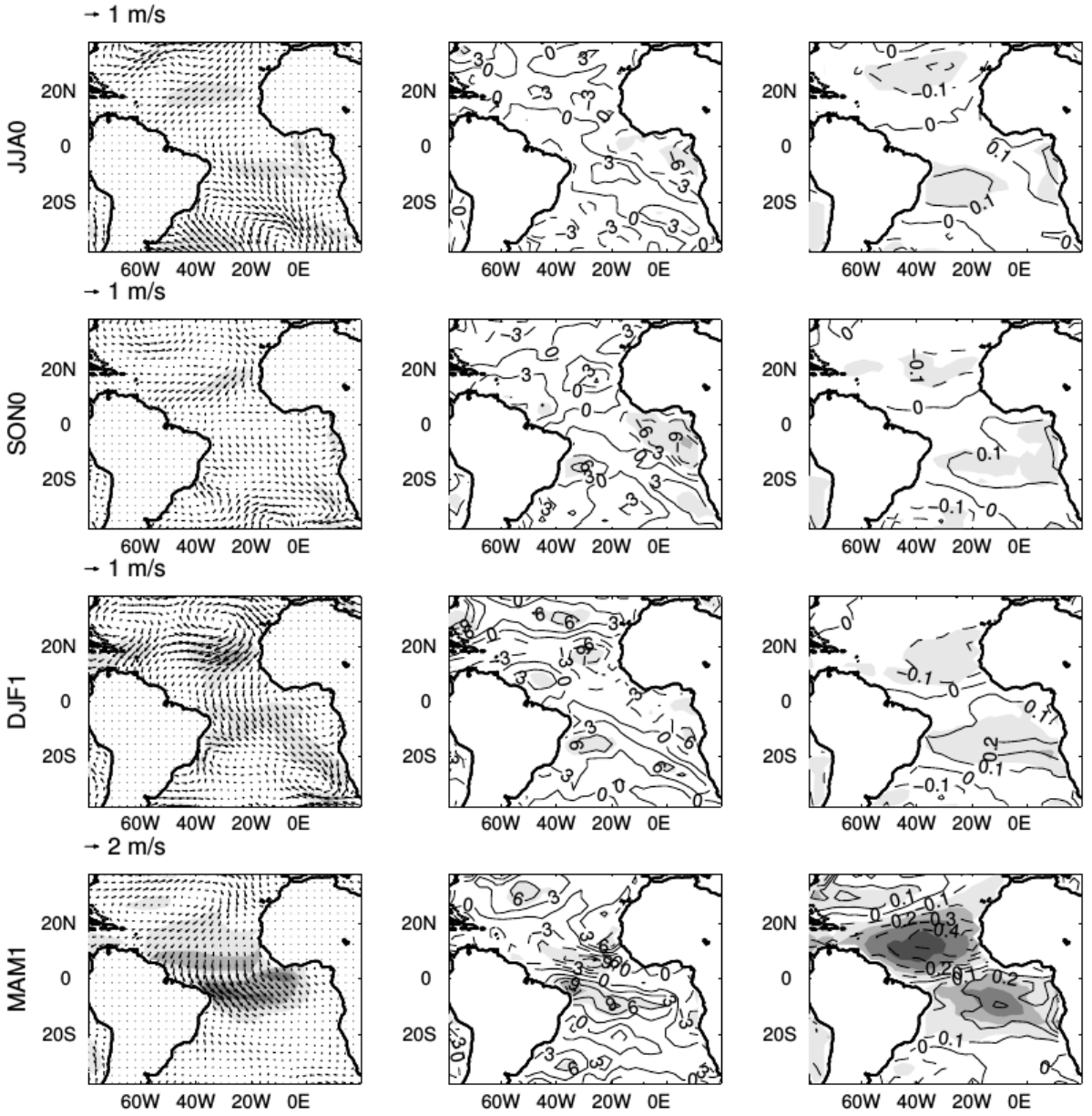

Figure 1. Lag-regression of 1000 hPa winds (left panels), surface downward heat flux (middle panels) and SST (right panels) anomaly onto the GI for seasons JJA0, SON0, DJF1 and MAM1. The GI index is constructed in MAM1. The regions used to construct the index are shown as boxes in the lower right panel. Arrows indicate the scale of 1000 hPa winds. The contour interval for heat flux is 3 W m^{-2}, and for SST is 0.1 K. Shading indicates the percentage of variance explained in intervals of 10%, 30%, 50%, and 70%. Explained variance of 10% is slightly above the 95% significance level. For surface winds the shading indicates explained variance in wind speed.

Barreiro et al 2004

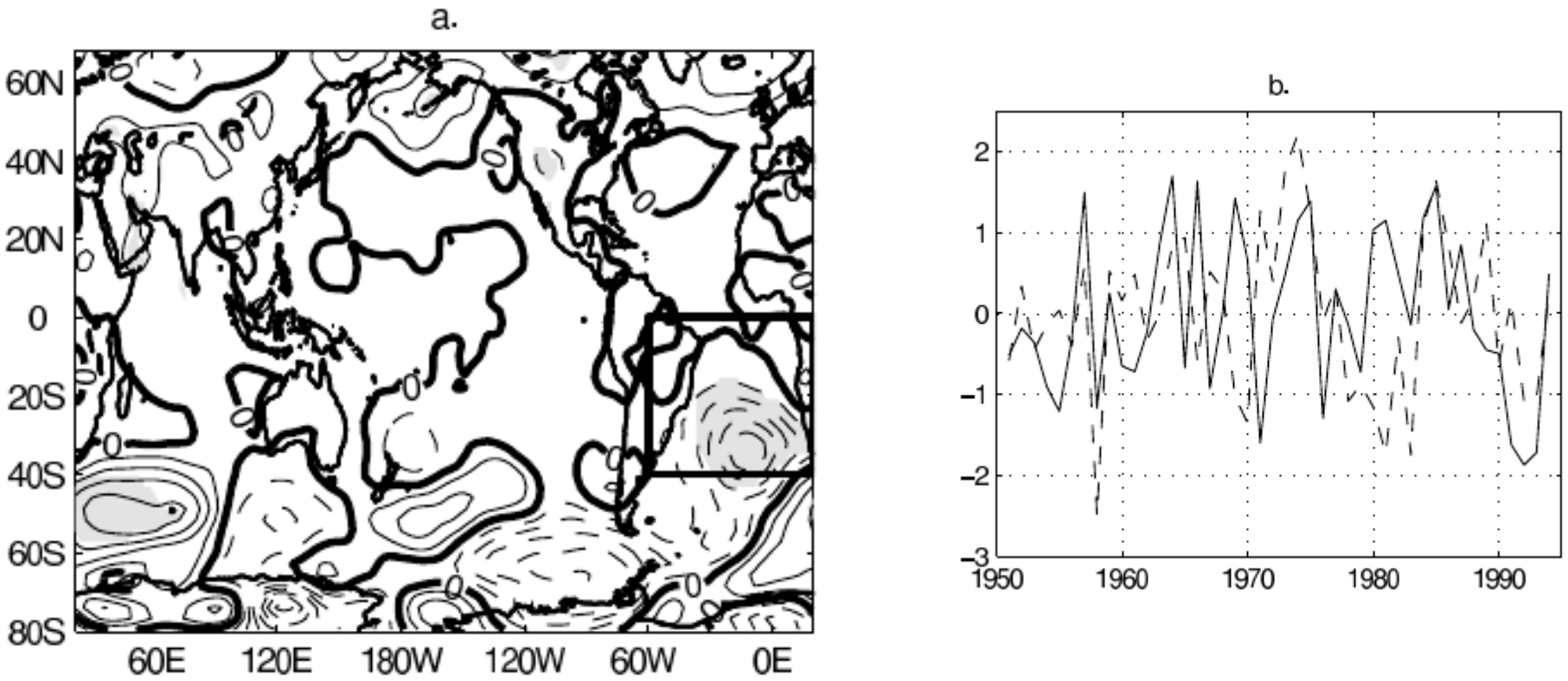

Figure 2. (a) Regression of sea level pressure onto the PC time series (P1JJAS) of winter-EOF during JJAS season. Spatial pattern of the leading mode of observed sea level The box marks the region in which the EOF analysis of 1000 hPa wind speed was performed. Contour interval is 20 Pa, and shading indicates significance at the 95% level. (b) Index P1JJAS (solid line) and GI time series (dashed line). P1JJAS is shifted 1-year so that it can be compared with GI index.

Figure 3. Same as Figure 1, but regressing onto the PC time series of the winter-EOF (P1JJAS) calculated in JJAS0.

OBS

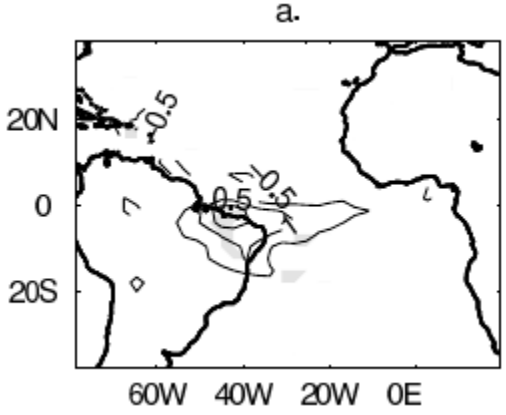

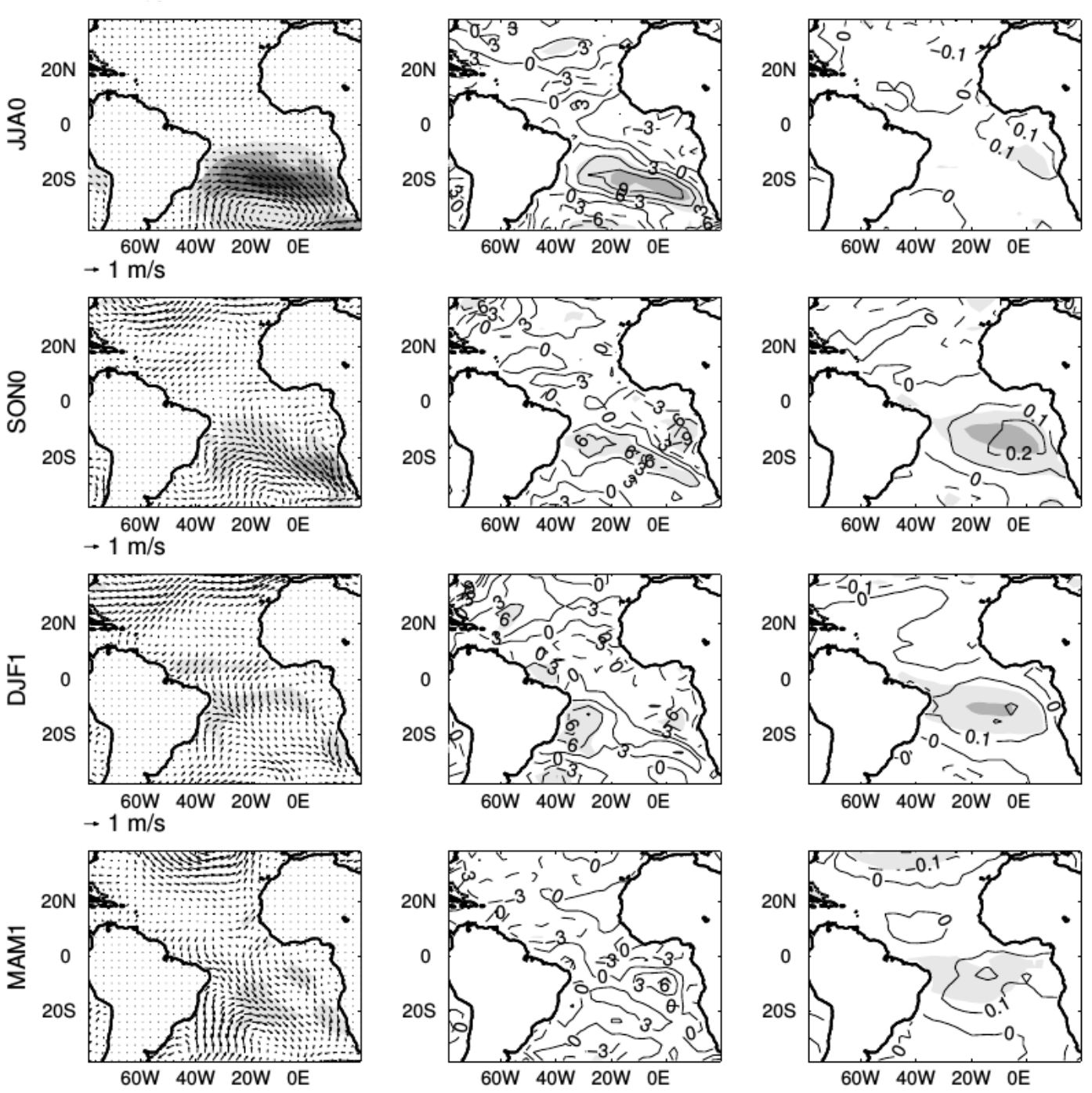

MODEL

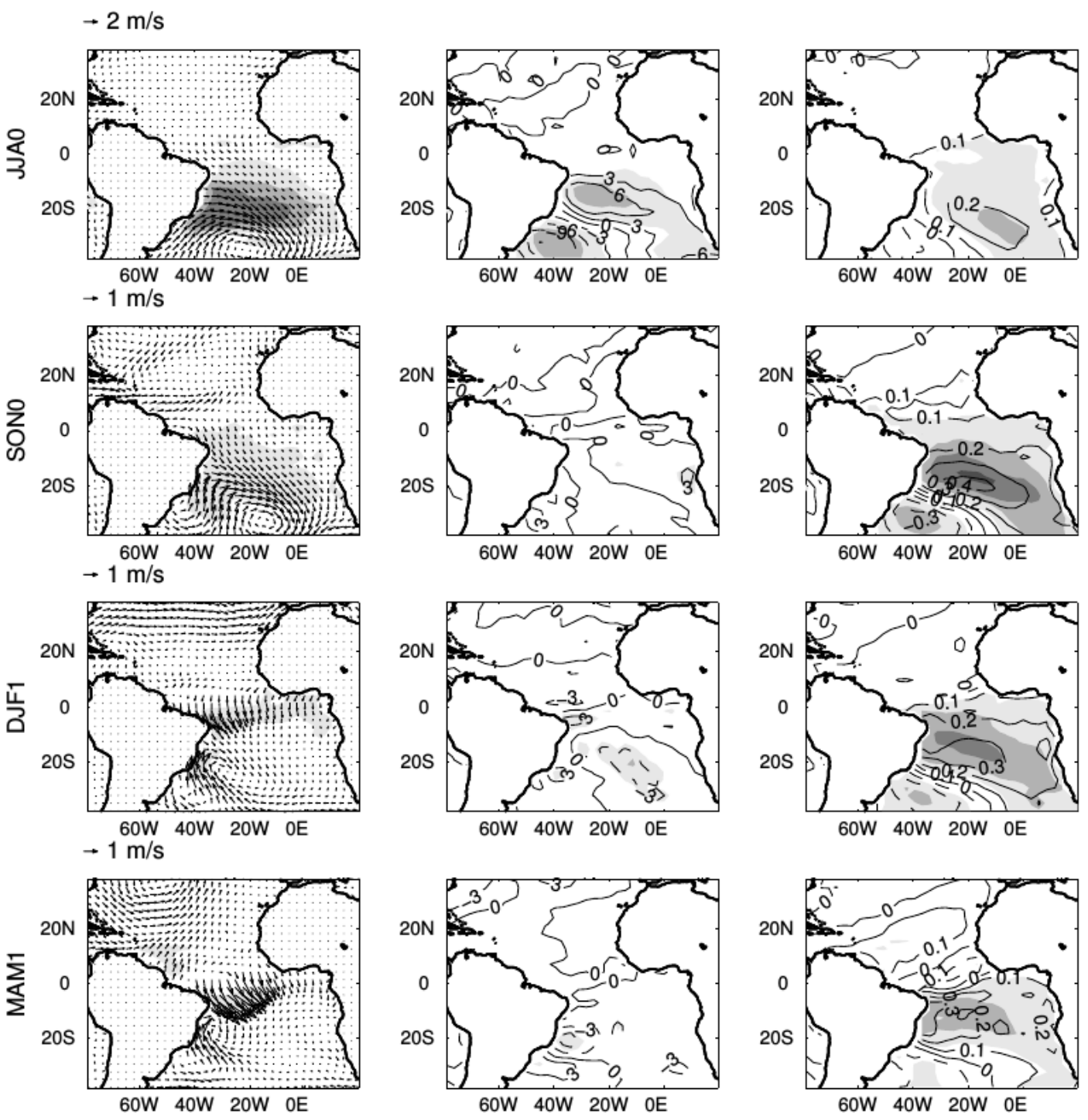

Figure 5. Same as Figure 3, but regressing onto the PC time series of the leading EOF of simulated wind-speed at 1000 hPa during JJAS0.

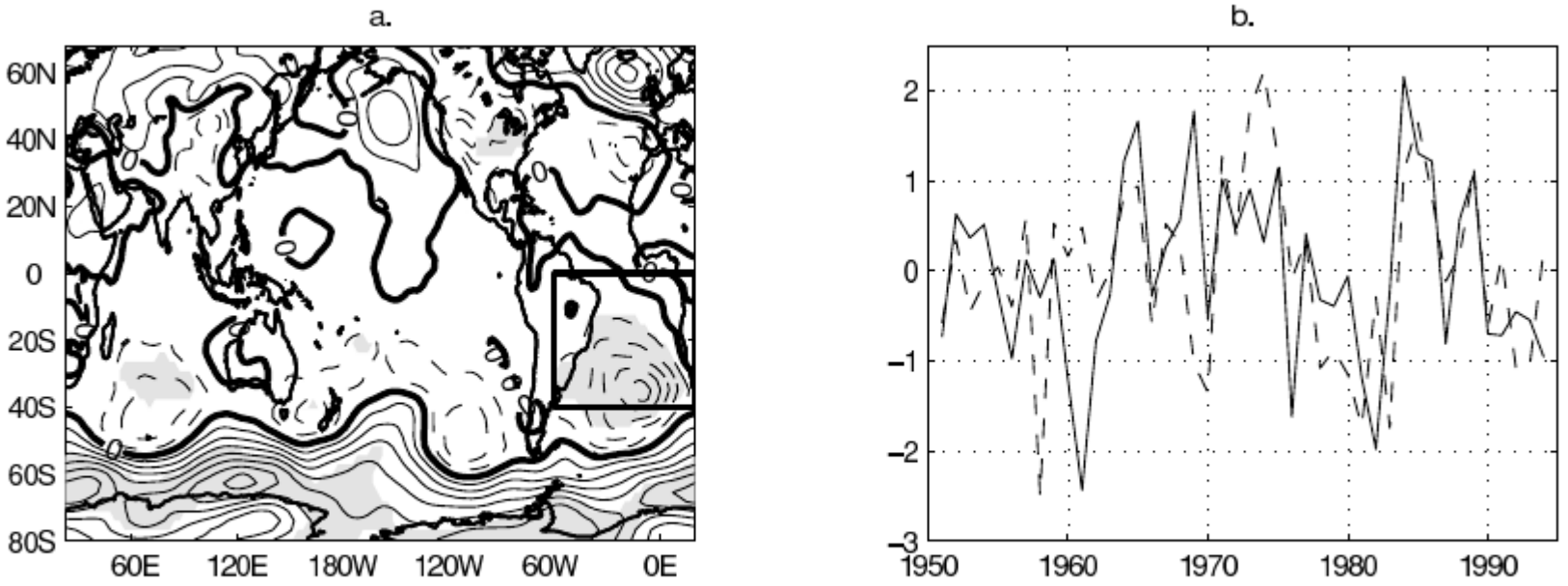

Figure 6. Same as Figure 2, but for the summer-EOF.

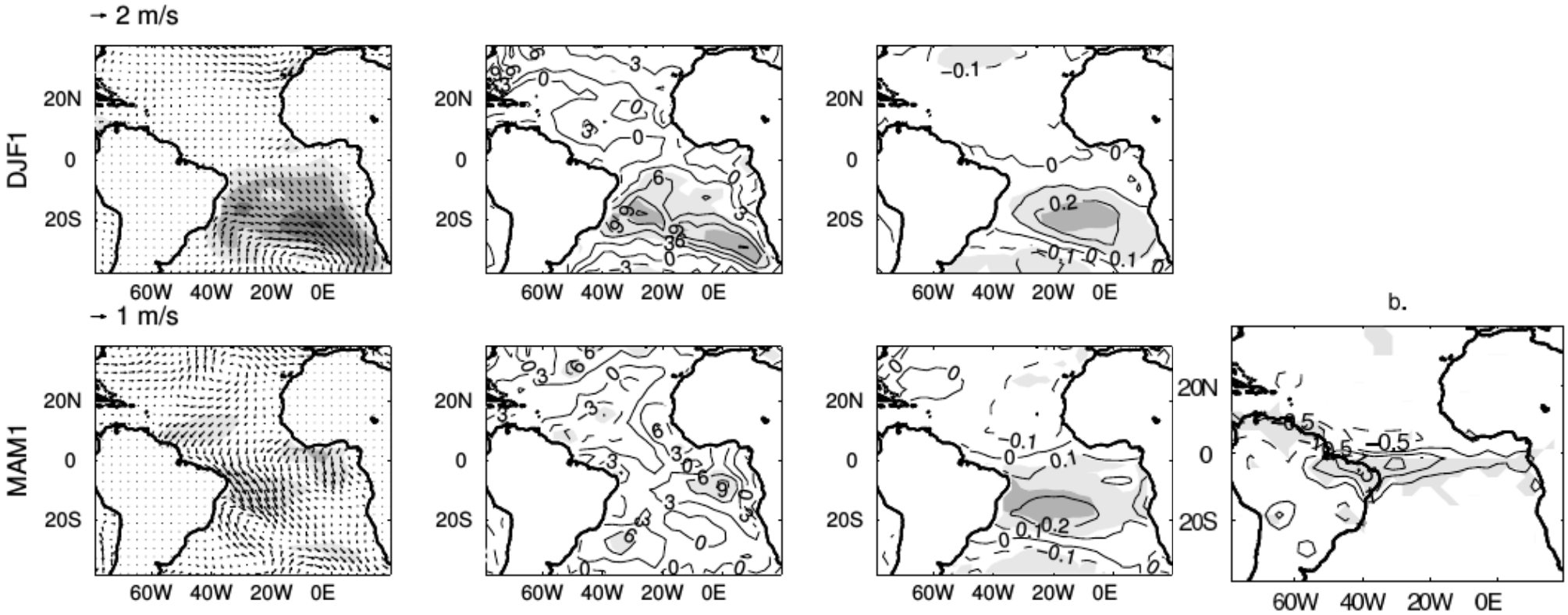

Figure 7. Lag-regression of 1000 hPa winds (left panels), surface downward heat flux (middle panels) and SST (right panels) anomaly onto the PC time series of summer-EOF (P1NDJF) for seasons DJF1 and MAM1. The P1NDJF index is constructed in NDJF1. Arrows indicate the scale of 1000 hPa winds. The contour interval for heat flux is 3 W m^{-2}, and for SST is 0.1 K. Shading indicates the percentage of variance explained in intervals of 10%, 30%, 50%, and 70%. Explained variance of 10% is slightly above the 95% significance level. For surface winds the shading indicates explained variance in wind speed.

Interacción océano-atmósfera en mesoescala

sampled. Analyses of these coarse-resolution ship observations in conjunction with coupled climate modeling on similarly coarse scales generally find a negative correlation between sea surface temperature (SST) and surface wind speed (Xie, 2004, and references therein). Except in the tropics, this interaction at large scales is interpreted as the ocean passively responding to wind-induced latent and sensible heat flux (i.e., a one-way forcing of the ocean by the atmosphere).

The advent of satellite-borne microwave radar scatterometers that measure the global surface wind field with a high spatial resolution of about 25 km, as described by Chelton and Freilich (2005), and microwave radiometers that measure SST in nearly all weather conditions with a spatial resolution of about 50 km, as described by Wentz et al. (2000) and Chelton and Wentz (2005), has revealed that ocean-atmosphere interaction is fundamentally different on oceanic mesoscales of 10–1000 km. Surface wind speed is found to be locally higher over warm water and lower over cool water (i.e., a positive correlation that is opposite to that found on large scales).

Chelton and Xie 2010

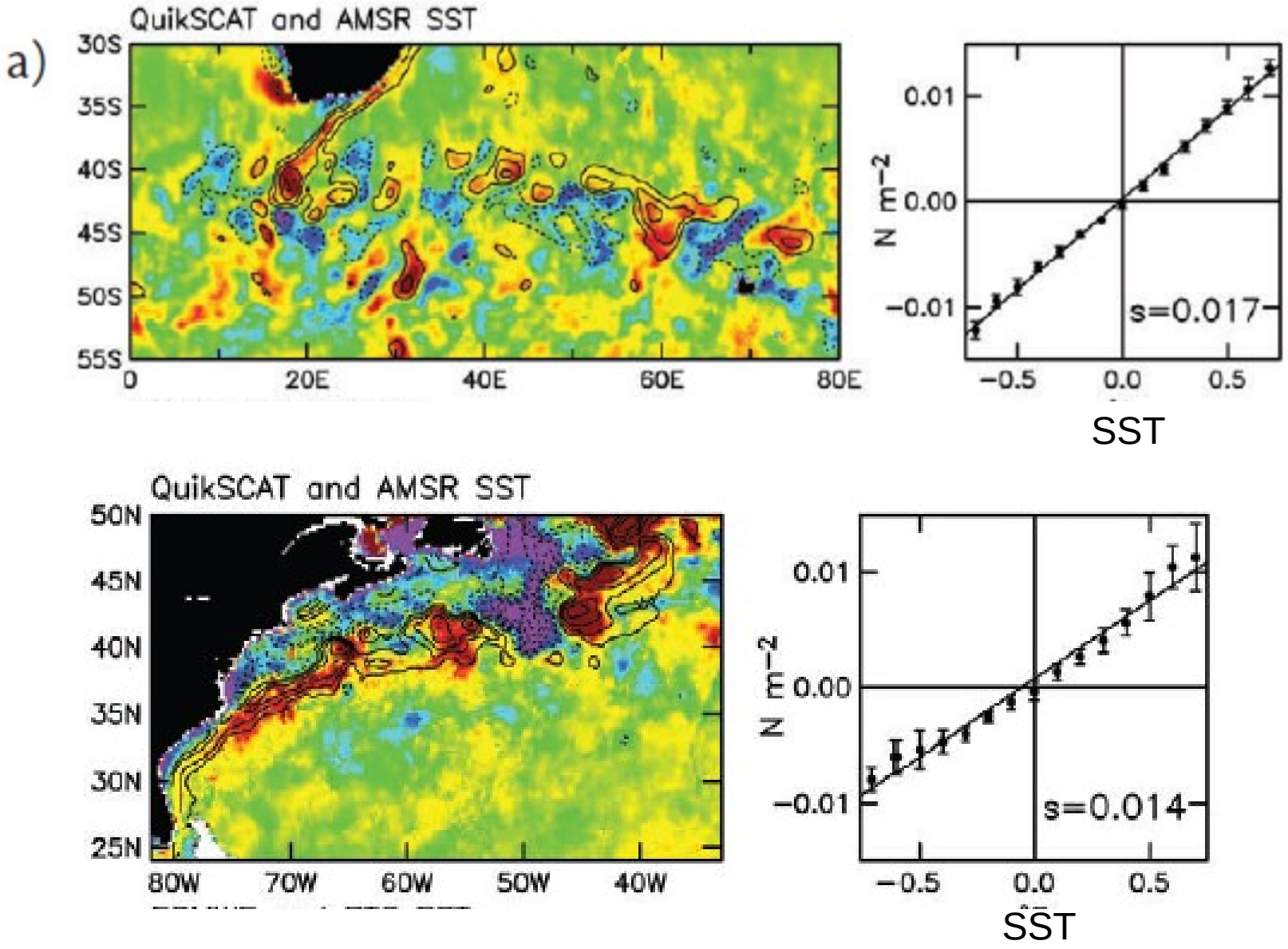

Figure 1. Maps and binned scatter plots for two-month averages (January–February 2008) of spatially high-pass-filtered sea surface temperature (SST; which has zero mean, by definition) overlaid as contours on spatially high-pass-filtered wind stress magnitude for the Agulhas Return Current region (left) and the Gulf Stream region (right). (a) QuikSCAT observations of wind stress and Advanced Microwave Scanning Radiometer (AMSR-E) observa-

2010). Changes in wind stress are mostly attributable to SST-induced changes in wind speed. Surface wind increases over warm water in association with decreased stability through enhanced vertical mixing by large eddies that deepen the boundary layer and draw momentum from the upper boundary layer down to the sea surface. Surface winds and wind stress decrease over cold water in association with increased stability that decouples the surface winds from the stronger winds aloft. Surface wind speed and stress are thus both positively correlated with SST (see, for example, Figures 1a and 4c).

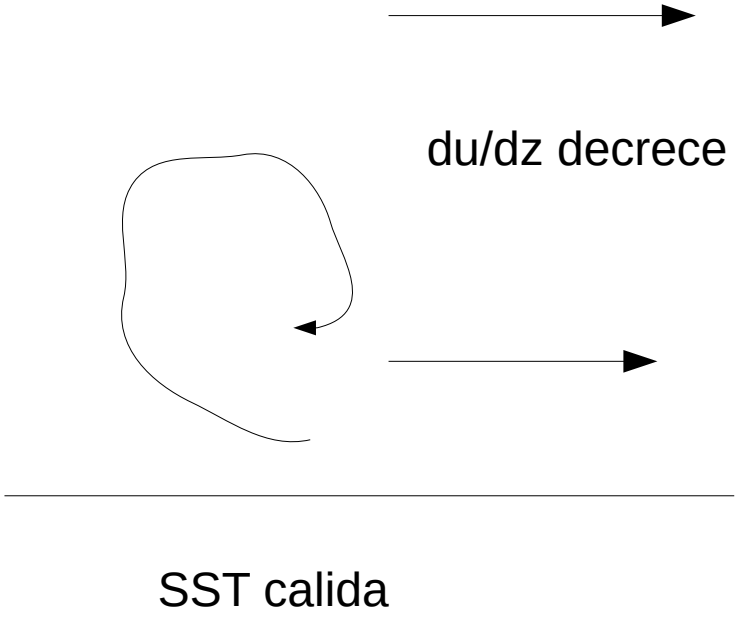

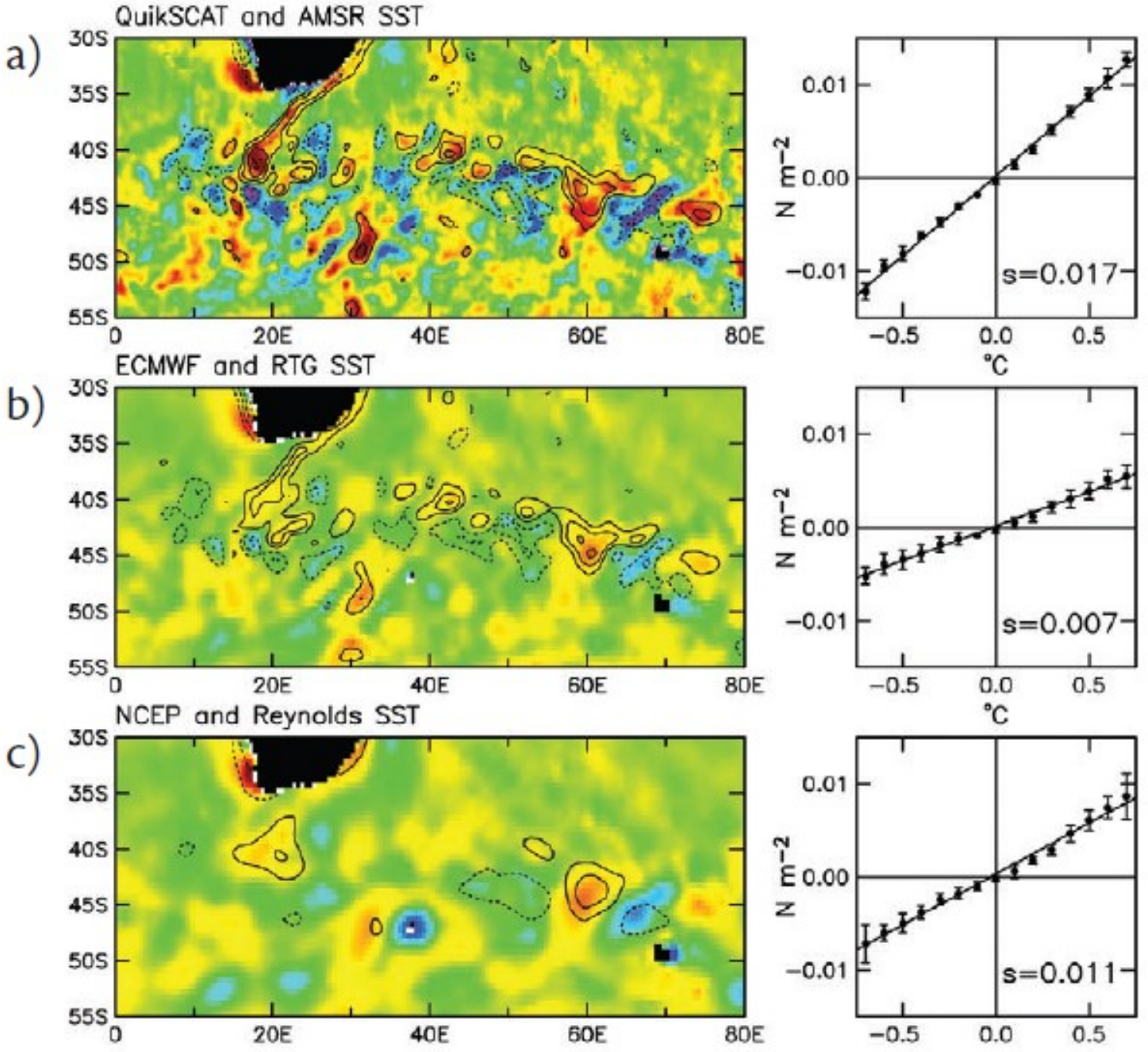
a)
QuikSCAT and AMSR SST
b)
ECMWF and RTG SST
c)
NCEP and Reynolds SST
30S
35S
40S
45S
50S
55S
0
20E
40E
60E
80E
0.01
0.00
−0.01
N m−2
−0.5
0.0
0.5
°C
s=0.017
s=0.007
s=0.011

Critical factors:Ocean resolution, vertical mixing in ABL and vertical resolution in ABL

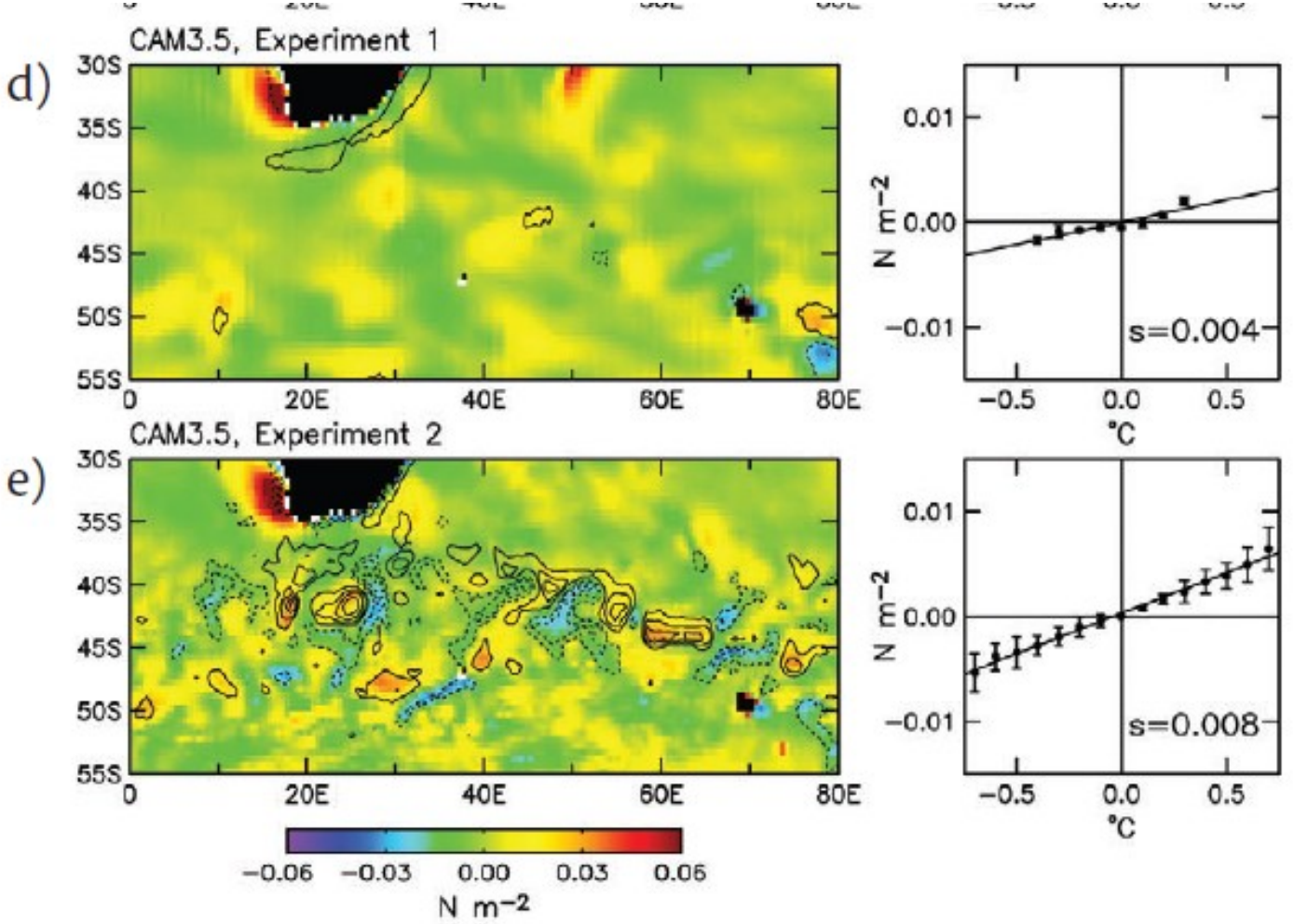

most other atmospheric models. Aside from the importance of the resolution of the SST boundary condition discussed above, the primary factor limiting the accuracy of the coupling appears to be the parameterization of vertical mixing.

the degree of underestimation of the coupling between SST and surface winds in models likely depends also on the models' vertical grid resolution.

tions of SST. (b) European Centre for Medium-range Weather Forecasts (ECMWF) wind stress and Real-Time Global (RTG) SST. (c) US National Centers for Environmental Prediction (NCEP) wind stress and Reynolds SST. (d) Wind stress and SST from the National Center for Atmospheric Research Community Climate System Model (NCAR CCSM3.5) coupled climate model with atmosphere and ocean grid resolutions of 0.5° and 1.125°, respectively. (e) Wind stress and SST from the same NCAR CCSM3.5 coupled climate model with atmosphere and ocean grid resolutions of 0.5° and 0.1°, respectively. Positive and negative high-pass filtered SST are shown as solid and dotted lines, respectively, with a contour interval of 1°C and with the zero contours omitted for clarity. The CCSM3.5 model simulations are not intended to represent actual years, so the two-month averages in panels d and e are for a representative January–February time period. The solid circles and error bars in the binned scatter plots are, respectively, the overall

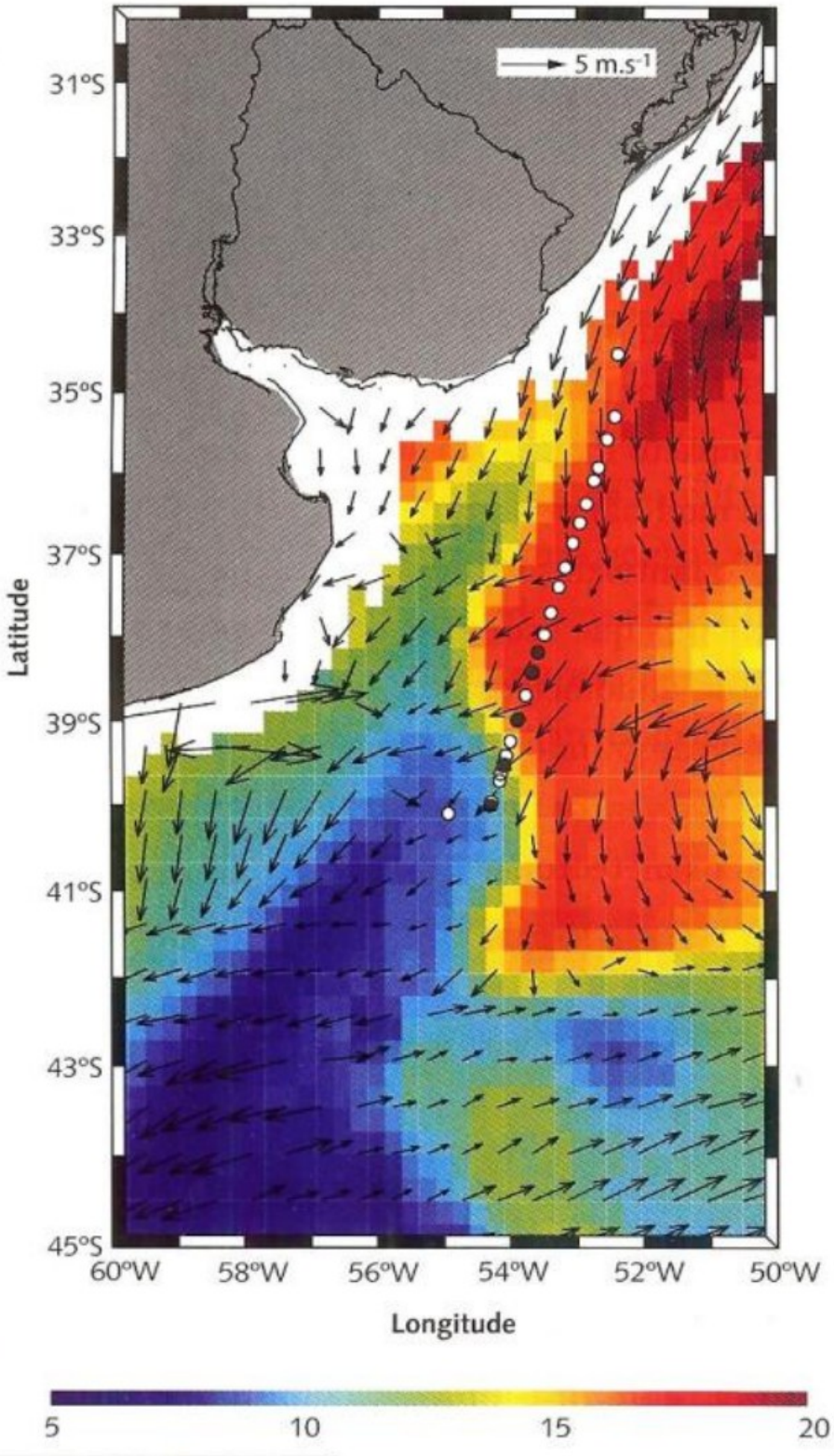

Fig. 24.9 Vetores de vento obtidos pelo escaterômetro a bordo do satélite QuikScat, no dia 2 de novembro de 2004, sobrepostos ao mapa de TSM (cores) obtido pelo sensor AMSR-E do satélite Aqua, na mesma data, na região da CBM. Indicam-se também as posições de lançamento de XBTs (pontos brancos) e radiossondas atmosféricas (pontos pretos) a partir do NApOc Ary Rongel, no dia 2 de novembro de 2004
Fonte: Pezzi et al., 2005.

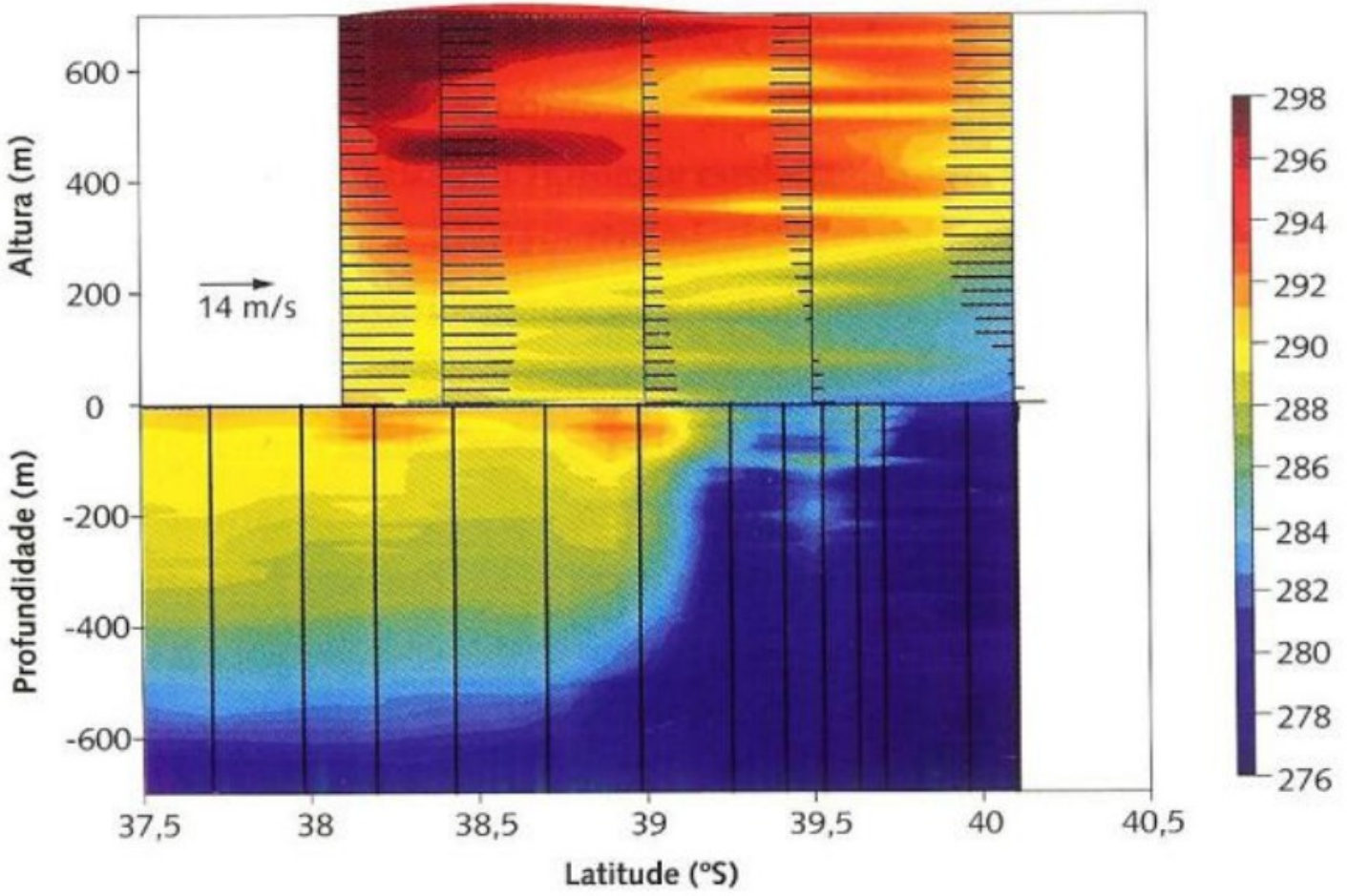

Fig. 24.10 Perfis simultâneos de temperatura da atmosfera e do oceano (K) medidos por radiossondas e XBTs ao longo da rota do NApOc Ary Rongel, de 1º a 3 de novembro de 2004. Os vetores de vento meridional ($m.s^{-1}$) são superimpostos aos campos de temperatura da atmosfera
Fonte: adaptado de Pezzi et al., 2005.

ventos próximos à superfície relativamente mais intensos. Conforme

A consequence of SST influence on surface winds is that spatial variability of SST generates divergence and curl of the surface wind field (Figure 2).

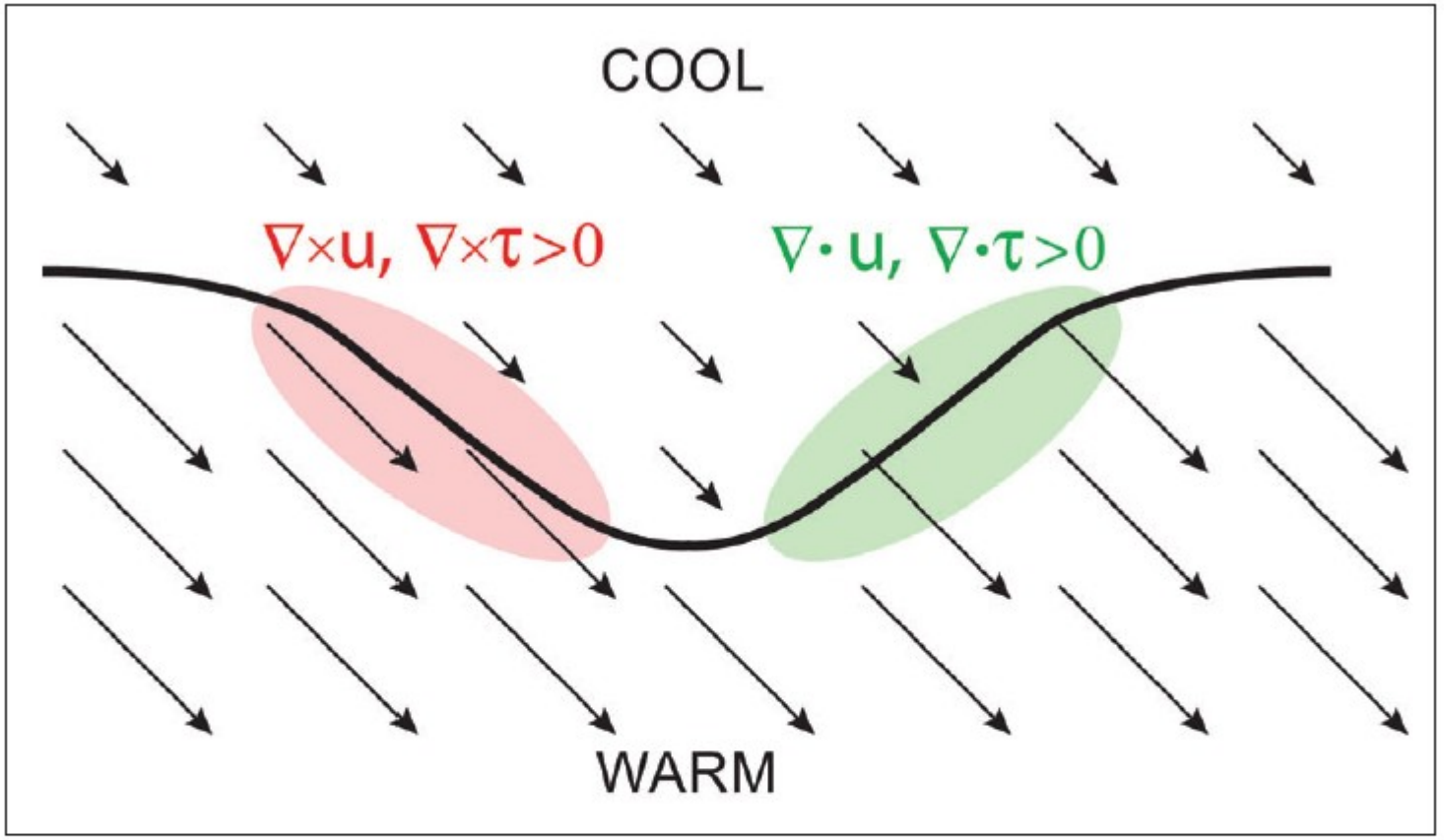

Figure 2. Schematic illustration of the divergence and curl of the wind and wind stress fields that result from spatial variations of the SST field. Near a meandering SST front (the heavy black line), surface winds are lower over cool water and higher over warm water, shown qualitatively by the lengths of the vectors. Acceleration where winds blow across the SST front generates divergence (green area). Lateral variations where winds blow parallel to the SST front generate curl (red area). The divergence and curl perturbations are proportional to the downwind and crosswind components of the SST gradient, respectively (see Figure 3).

The divergence and curl responses to spatially varying SST have important implications for both the atmosphere and the ocean. In the case of the atmosphere, SST influence can penetrate into the troposphere from the vertical motion induced by convergence and divergence of the surface wind field. In the case of the ocean, the upwelling and downwelling that are associated with the wind stress curl alter the ocean circulation, and therefore the SST itself.

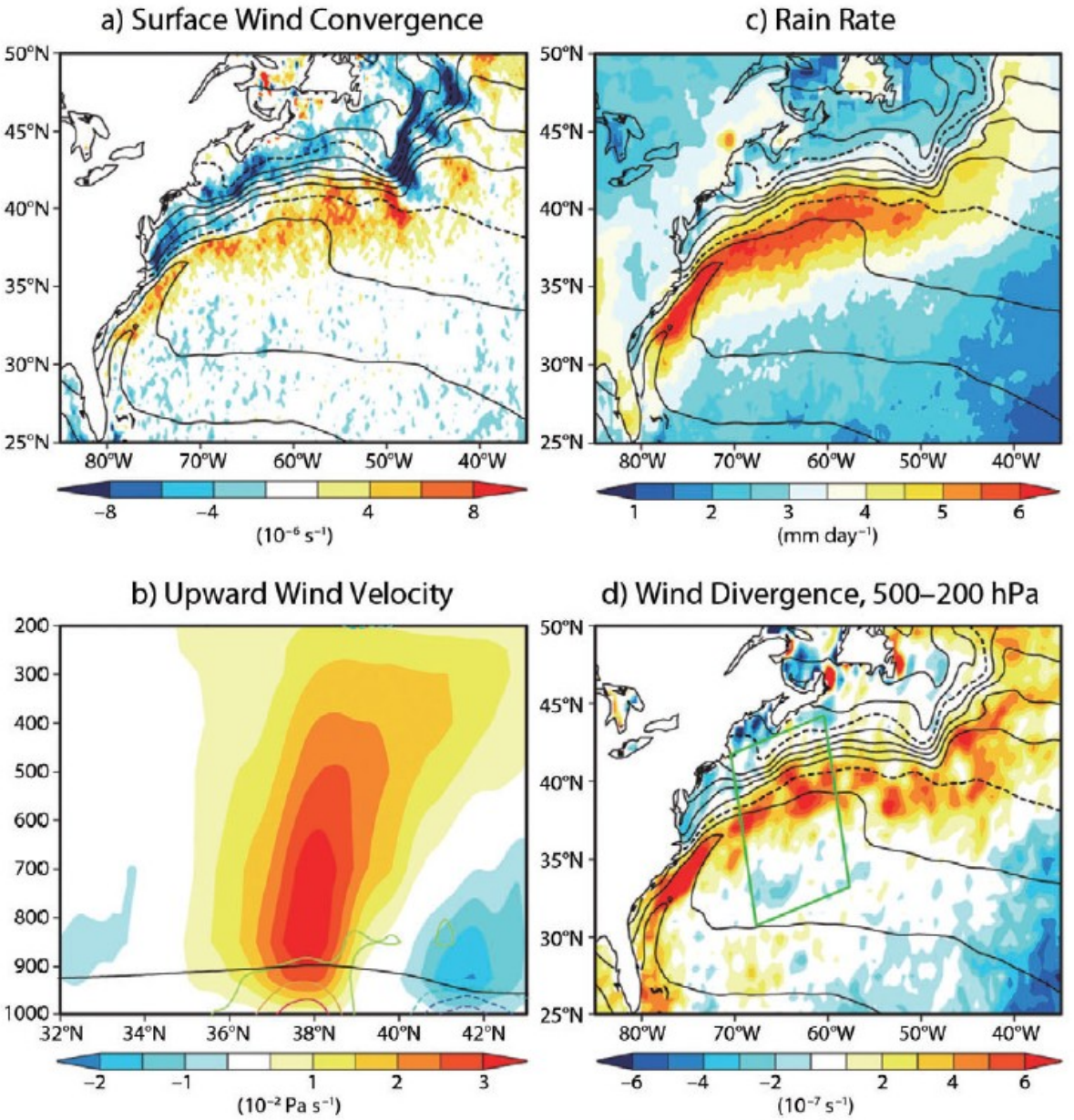

Figure 5. Annual means of (a) surface wind convergence from QuikSCAT observations of surface winds, (b) vertical velocity in pressure coordinates from the ECMWF model, (c) rain rate from the Tropical Rainfall Measuring Mission satellite observations, and (d) upper-tropospheric divergence from the ECMWF model averaged over the pressure range 500–200 hPa. The contours in panels a, c, and d show SST with a contour interval of 2°C. The black line in panel b is the boundary layer height, and the other contours plot wind convergence averaged in the along-front direction across the green box in panel d with a contour interval of 10^{-6} s^{-1} (solid for convergence and dashed for divergence, with the zero contours omitted for clarity). *Modified from Minobe et al. (2008)*

circulation. In atmospheric models, spatial smoothing of the SST boundary condition significantly changes storm-track activity in these regions (Taguchi et al., 2009; Kuwano-Yoshida et al., 2010). A high-resolution SST boundary condition is therefore crucially important for weather forecast models to represent this cyclogenesis accurately. By energizing storms, a sharp SST front in the mid latitudes can anchor the axis of westerly winds at the sea surface (Nakamura et al., 2008). These surface westerlies can then feed back on ocean circulation, strengthening the flow and the SST front itself.

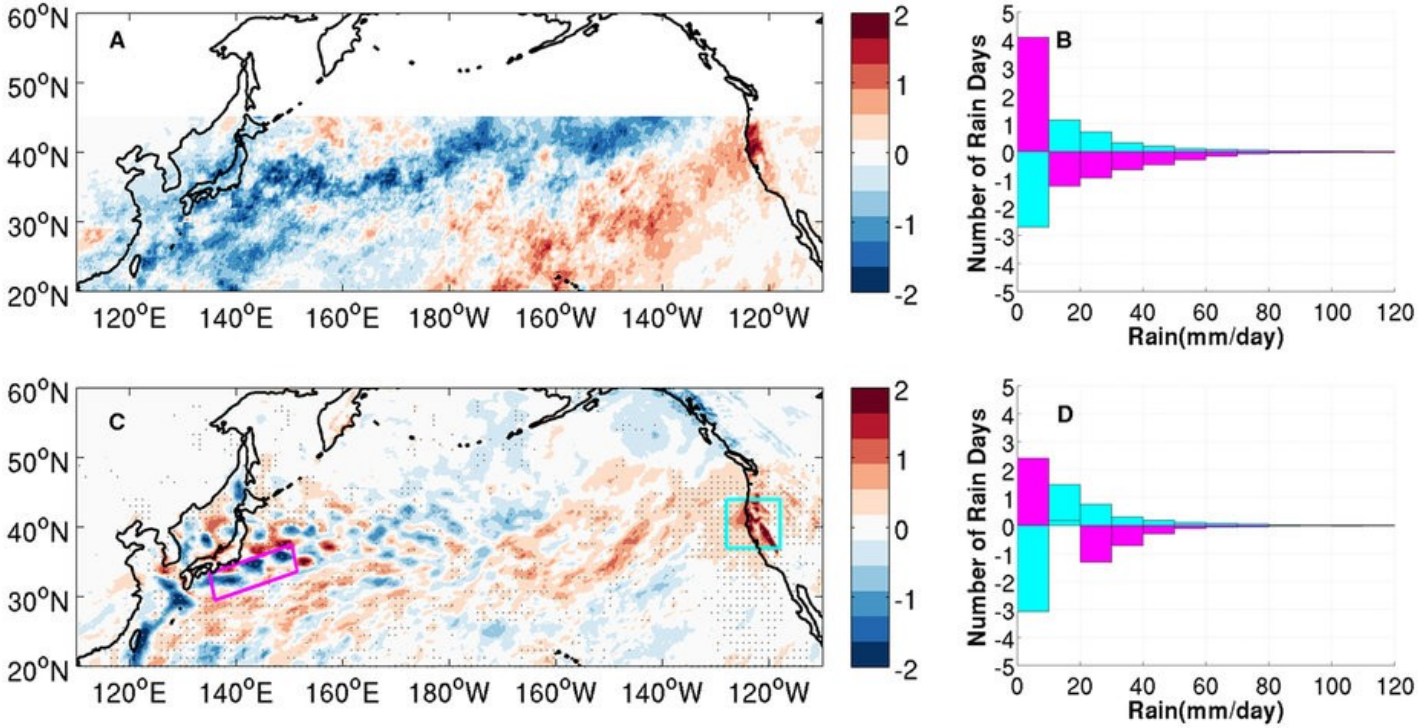

(A) Difference of TRMM winter season (NDJFM) mean rainfall (mmd−1) between Inactive Eddy Years (IEYs) and Active Eddy Years (AEY). (B) TRMM daily rainfall PDF difference between IEYs and AEYs along the Kuroshio (magenta) and over the U.S. North Pacific coast (cyan). (C) Difference of winter season (NDJFM) mean total rainfall (mmd−1) between two ensembles of 10 WRF simulations, MEFS (without ocean eddies) and CTRL (with ocean eddies). Rainfall difference significant at 95% confidence level based on a two-sided Wilcoxon rank sum test is shaded by gray dots. (D) Daily rainfall PDF difference between MEFS and CTRL along Kuroshio (magenta) and over the U.S. North Pacific coast (cyan). For both TRMM3B42 and simulated rainfiall, the PDF was derived by counting the number of rainy days in different rain rate ranges at each grid point and then averaging them in the region along the Kuroshio (denoted by the magenta box in (C)) and over the U.S. North Pacific coast (denoted by the cyan box in (C)). The maps were generated using M_Map V1.4 package for Matlab (http://www.eos.ubc.ca/~rich/map.html).

Ma et al 2015

RegESM

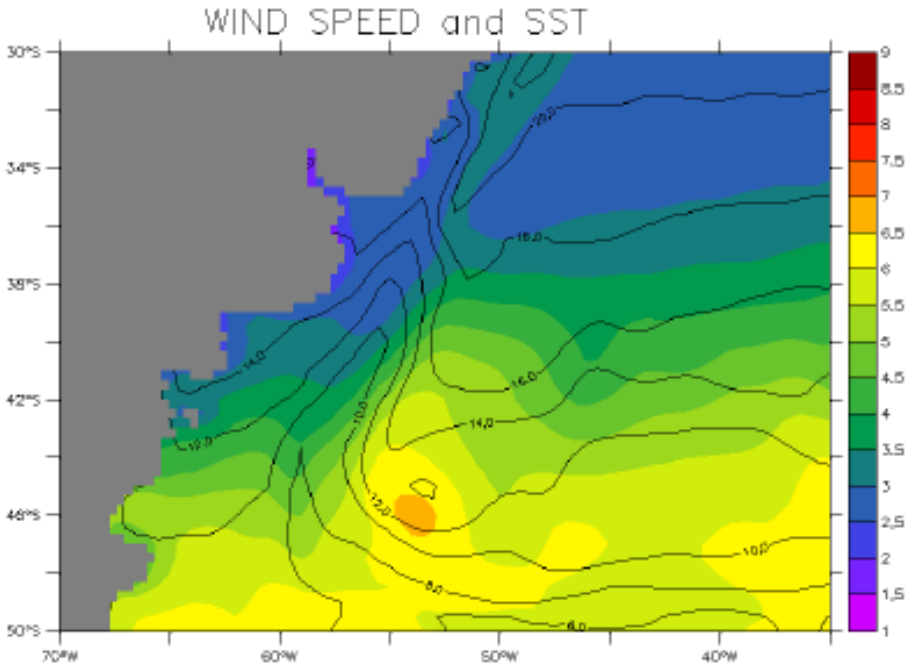
WIND SPEED and SST
30°S
34°S
38°S
42°S
46°S
50°S
70°W
60°W
50°W
40°W

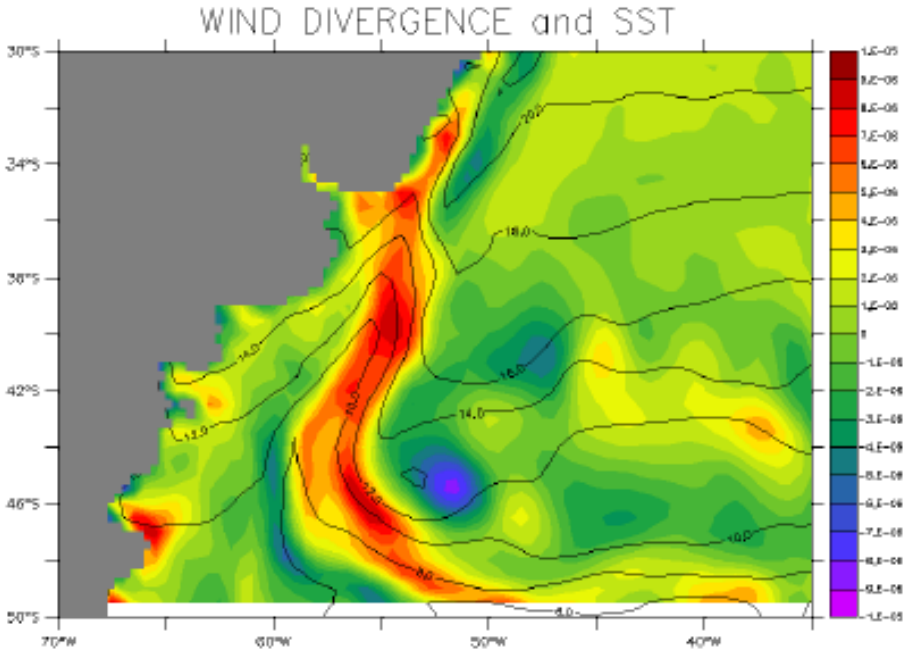
WIND DIVERGENCE and SST
30°S
34°S
38°S
42°S
46°S
50°S
70°W
60°W
50°W
40°W

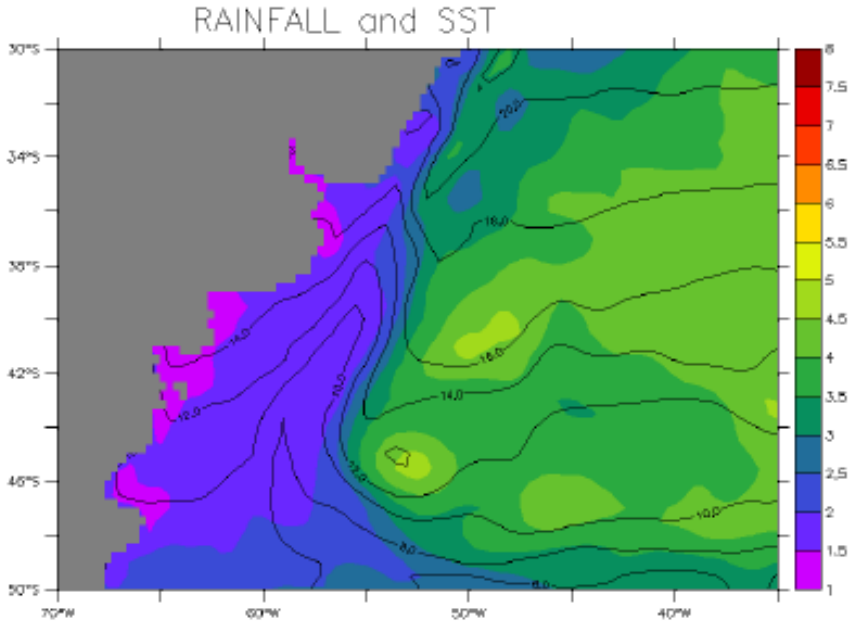
RAINFALL and SST
30°S
34°S
38°S
42°S
46°S
50°S
70°W
60°W
50°W
40°W

The end!